DOI: 10.1126/science.abn8671

Submitted Manuscript: Confidential
Template revised February 2021

Formation and evolution of carbonaceous asteroid Ryugu: Direct evidence from returned samples

T. Nakamura[1]*, M. Matsumoto[1], K. Amano[1], Y. Enokido[1], M. E. Zolensky[2], T. Mikouchi[3], H. Genda[4], S. Tanaka[5,6], M. Y. Zolotov[7], K. Kurosawa[8], S. Wakita[9], R. Hyodo[5], H. Nagano[10], D. Nakashima[1], Y. Takahashi[11], Y. Fujioka[1], M. Kikuiri[1], E. Kagawa[1], M. Matsuoka[12,13], A. J. Brearley[14], A. Tsuchiyama[15,16,17], M. Uesugi[18], J. Matsuno[15], Y. Kimura[19], M. Sato[11], R. E. Milliken[20], E. Tatsumi[21,11], S. Sugita[11,8], T. Hiroi[20], K. Kitazato[22], D. Brownlee[23], D. J. Joswiak[23], M. Takahashi[1], K. Ninomiya[24], T. Takahashi[25,26], T. Osawa[27], K. Terada[28], F. E. Brenker[29], B. J. Tkalcec[29], L. Vincze[30], R. Brunetto[31], A. Aléon-Toppani[31], Q. H. S. Chan[32], M. Roskosz[33], J.-C. Viennet[33], P. Beck[34], E. E. Alp[35], T. Michikami[36], Y. Nagaashi[37,1], T. Tsuji[38,39], Y. Ino[40,5], J. Martinez[2], J. Han[41], A. Dolocan[42], R. J. Bodnar[43], M. Tanaka[44], H. Yoshida[11], K. Sugiyama[45], A. J. King[46], K. Fukushi[47], H. Suga[18], S. Yamashita [48,49], T. Kawai[11], K. Inoue[47], A. Nakato[5], T. Noguchi[50,51], F. Vilas[52], A. R. Hendrix[53], C. Jaramillo[54], D. L. Domingue[52], G. Dominguez[55], Z. Gainsforth[56], C. Engrand[57], J. Duprat[33], S. S. Russell[46], E. Bonato[58], C. Ma[59], T. Kawamoto[60], T. Wada[1], S. Watanabe[5,25], R. Endo[61], S. Enju[62], L. Riu[63], S. Rubino[31], P. Tack[30], S. Takeshita[64], Y. Takeichi[48,49], A. Takeuchi[18], A. Takigawa[11], D. Takir[2], T. Tanigaki[65], A. Taniguchi[66], K. Tsukamoto[1], T. Yagi[67], S. Yamada[68], K. Yamamoto[69], Y. Yamashita[67], M. Yasutake[18], K. Uesugi[18], I. Umegaki[70,64], I. Chiu[24], T. Ishizaki[5], S. Okumura[50], E. Palomba[72], C. Pilorget[31,73], S. M. Potin[12], A. Alasli[10], S. Anada[69], Y. Araki[74], N. Sakatani[68,5], C. Schultz[20], O. Sekizawa[18], S. D. Sitzman[75], K. Sugiura[4], M. Sun[16,17,76], E. Dartois[77], E. De Pauw[30], Z. Dionnet[31], Z. Djouadi[31], G. Falkenberg[78], R. Fujita[10], T. Fukuma[79], I. R. Gearba[42], K. Hagiya[80], M. Y. Hu[35], T. Kato[69], T. Kawamura[81], M. Kimura[48,49], M. K. Kubo[82], F. Langenhorst[83], C. Lantz[31], B. Lavina[84] , M. Lindner[29], J. Zhao[35], B. Vekemans[30], D. Baklouti[31], B. Bazi[30], F. Borondics[85], S. Nagasawa[25, 26], G. Nishiyama[11], K. Nitta[18], J. Mathurin[86], T. Matsumoto[50], I. Mitsukawa[50], H. Miura[87], A. Miyake[50], Y. Miyake[64], H. Yurimoto[88], R. Okazaki[89], H. Yabuta[90], H. Naraoka[89], K. Sakamoto[5], S. Tachibana[11,5], H. C. Connolly Jr.[91], D. S. Lauretta[92], M. Yoshitake[5], M. Yoshikawa[5,6], K. Yoshikawa[92], K. Yoshihara[5], Y. Yokota[5], K. Yogata[5], H. Yano[5,6], Y. Yamamoto[5,6], D. Yamamoto[5], M. Yamada[8], T. Yamada[5], T. Yada[5], K. Wada[8], T. Usui[5,11], R. Tsukizaki[5], F. Terui[94], H. Takeuchi[5,6], Y. Takei[5], A. Iwamae[95], H. Soejima[5,95], K. Shirai[5], Y. Shimaki[5], H. Senshu[8], H. Sawada[5], T. Saiki[5], M. Ozaki[5,6], G. Ono[93] T. Okada[5,11], N. Ogawa[5], K. Ogawa[5], R. Noguchi[96], H. Noda[97], M. Nishimura[5], N. Namiki[97,6], S. Nakazawa[5], T. Morota[11], A. Miyazaki[5], A. Miura[5], Y. Mimasu[5], K. Matsumoto[97,6], K. Kumagai[5,95], T. Kouyama[98], S. Kikuchi[8,97], K. Kawahara[5], S. Kameda[68,5], T. Iwata[5,6], Y. Ishihara[99], M. Ishiguro[100], H. Ikeda[93], S. Hosoda[5], R. Honda[101,102], C. Honda[22], Y. Hitomi[5,95], N. Hirata[37], N. Hirata[22], T. Hayashi[5], M. Hayakawa[5], K. Hatakeda[5,95], S. Furuya[11], R. Fukai[5], A. Fujii[5], Y. Cho[11], M. Arakawa[37], M. Abe[5,6], S. Watanabe[103], Y. Tsuda[5].

Affiliations:

[1]Department of Earth Sciences, Tohoku University, Sendai 980-8578, Japan.

*Corresponding author. Email: tomoki.nakamura.a8@tohoku.ac.jp

[2]NASA Johnson Space Center; Houston TX 77058, USA.

[3]The University Museum, The University of Tokyo, Tokyo 113-0033, Japan.

[4]Earth-Life Science Institute, Tokyo Institute of Technology, Tokyo 152-8550, Japan.

[5]Institute of Space and Astronautical Science, Japan Aerospace Exploration Agency (JAXA), Sagamihara 252-5210, Japan.

[6]Department of Space and Astronautical Science, The Graduate University for Advanced Studies (SOKENDAI), Hayama 240-0193, Japan.
[7]School of Earth and Space Exploration, Arizona State University, Tempe AZ 85287, USA.
[8]Planetary Exploration Research Center, Chiba Institute of Technology, Narashino 275-0016, Japan.
[9]Department of Earth, Atmospheric and Planetary Sciences, Massachusetts Institute of Technology, Cambridge MA 02139, USA.
[10]Department of Mechanical Systems Engineering, Nagoya University, Nagoya 464-8603, Japan.
[11]Department of Earth and Planetary Science, The University of Tokyo, Tokyo 113-0033, Japan.
[12]Laboratoire d'Etudes Spatiales et d'Instrumentation en Astrophysique (LESIA), Observatoire de Paris, Meudon 92195 France
[13]Geological Survey of Japan, National Institute of Advanced Industrial Science and Technology (AIST), Tsukuba, 305-8567, Japan.
[14]Department of Earth and Planetary Sciences, University of New Mexico, Albuquerque NM 87131, USA.
[15]Research Organization of Science and Technology, Ritsumeikan University, Kusatsu 525-8577, Japan.
[16]Guangzhou Institute of Geochemistry, Chinese Academy of Sciences (CAS), Guangzhou 510640, China.
[17]CAS Center for Excellence in Deep Earth Science, Guangzhou 510640, China.
[18]Research and Utilization Division, Japan Synchrotron Radiation Research Institute, Sayo 679-5198, Japan.
[19]Institute of Low Temperature Science, Hokkaido University, Sapporo 060-0819, Japan.
[20]Department of Earth, Environmental, and Planetary Sciences, Brown University, Providence, RI 02912, USA.
[21]Instituto de Astrofísica de Canarias, University of La Laguna, Tenerife 38205, Spain.
[22]Aizu Research Center for Space Informatics, The University of Aizu, Aizu-Wakamatsu 965-8580, Japan.
[23]Department of Astronomy, University of Washington, Seattle WA 98195 USA.
[24]Institute for Radiation Sciences, Osaka University, Toyonaka 560-0043, Japan.
[25] Kavli Institute for the Physics and Mathematics of the Universe (The World Premier International Research Center Initiative), The University of Tokyo, Kashiwa 277-8583, Japan.
[26]Department of Physics, The University of Tokyo, Tokyo 113-0033, Japan.
[27]Materials Sciences Research Center, Japan Atomic Energy Agency, Tokai 319-1195, Japan.
[28]Department of Earth and Space Science, Osaka University; Toyonaka 560-0043, Japan.
[29]Institute of Geoscience, Goethe University, Frankfurt, 60438 Frankfurt am Main, Germany.
[30]Department of Chemistry, Ghent University, Krijgslaan 281 S12, Ghent, Belgium.
[31]Institut d'Astrophysique Spatiale, Université Paris-Saclay, Orsay 91405, France.
[32]Department of Earth Sciences, Royal Holloway University, Egham TW20 0EX, UK.
[33] Institut de Minéralogie, Physique des Matériaux et Cosmochimie, Muséum National d'Histoire Naturelle, Sorbonne Université, Paris, France.
[34]Institut de Planétologie et d'Astrophysique de Grenoble, Centre national de la recherche scientifique (CNRS), Université Grenoble Alpes, 38000 Grenoble, France.
[35]Advanced Photon Source, Argonne National Laboratory, Argonne, IL 60439, USA.
[36]Department of Mechanical Engineering, Kindai University, Higashi-Hiroshima 739-2116, Japan.
[37]Department of Planetology, Kobe University, Kobe 657-8501, Japan.
[38]Department of Earth Resources Engineering, Kyushu University, Fukuoka 819-0395, Japan.
[39]School of Engineering, The University of Tokyo, Tokyo 113-0033, Japan.
[40]Department of Physics, Kwansei Gakuin University, Sanda 669-1337, Japan.
[41]Department of Earth and Atmospheric Sciences, University of Houston, Houston TX 77204, USA.
[42]Texas Materials Institute, The University of Texas at Austin, Austin TX 78712, USA.

[43]Department of Geoscience, Virginia Tech., Blacksburg VA 24061, USA.
[44]Materials Analysis Station, National Institute for Materials Science, Tsukuba 305-0047, Japan.
[45]Institute for Materials Research, Tohoku University, Sendai 980-8577, Japan.
[46]Department of Earth Science, Natural History Museum, London SW7 5BD, UK.
[47]Institute of Nature and Environmental Technology, Kanazawa University, Kanazawa 920-1192, Japan.
[48]Department of Materials Structure Science, The Graduate University for Advanced Studies (SOKENDAI), Tsukuba, Ibaraki 305-0801, Japan.
[49]Institute of Materials Structure Science, High-Energy Accelerator Research Organization, Tsukuba 305-0801, Japan.
[50]Division of Earth and Planetary Sciences, Kyoto University; Kyoto 606-8502, Japan
[51]Faculty of Arts and Science, Kyushu University, Fukuoka 819-0395, Japan.
[52]Planetary Science Institute, Seabrook TX 77586, USA.
[53]Planetary Science Institute, Tucson AZ 85719, USA.
[54]The Pennsylvania State University, University Park, PA 16802, USA.
[55]Department of Physics, California State University, San Marcos, CA 92096, USA.
[56]Space Sciences Laboratory, University of California, California 94720, USA.
[57]Laboratoire de Physique des 2 Infinis Irène Joliot-Curie, Université Paris-Saclay, CNRS, 91405 Orsay, France.
[58]Institute for Planetary Research, Deutsches Zentrum für Luftund Raumfahrt, Rutherfordstraße 2 12489 Berlin, Germany.
[59]California Institute of Technology, Pasadena CA 91125, USA.
[60]Faculty of Science, Shizuoka University, Shizuoka 422-8529, Japan.
[61]Department of Materials Science and Engineering, Tokyo Institute of Technology, Tokyo 152-8550, Japan.
[62]Graduate School of Science and Engineering, Ehime University, Matsuyama 790-8577, Japan.
[63]European Space Astronomy Centre, 28692 Villanueva de la Cañada, Spain.
[64]High Energy Accelerator Research Organization, Tokai 319-1106, Japan.
[65]Hitachi, Ltd., Hatoyama 350-0395, Japan.
[66]Institute for Integrated Radiation and Nuclear Science, Kyoto University, Kumatori 590-0494, Japan.
[67]National Metrology Institute of Japan, AIST, Tsukuba 305-8565, Japan.
[68]Department of Physics, Rikkyo University, Tokyo 171-8501, Japan.
[69]Japan Fine Ceramics Center, Nagoya 456-8587, Japan.
[70]Toyota Central Research and Development Laboratories, Inc., Nagakute 480-1192, Japan.
[7172]Istituto di Astrofisica e Planetologia Spaziali, Istituto, Nazionale di Astrofisica, Rome 00133, Italy.
[73]Institut Universitaire de France, Paris, France.
[74]Department of Physical Sciences, Ritsumeikan University, Shiga 525-0058, Japan.
[75]Physical Sciences Laboratory, The Aerospace Corporation, California 90245, USA.
[76]University of Chinese Academy of Sciences, Beijing 100049, China.
[77]Institut des Sciences Moléculaires d'Orsay, Université Paris-Saclay, CNRS, 91405 Orsay, France.
[78]Deutsches Elektronen-Synchrotron Photon Science, 22603 Hamburg, Germany.
[79]Nano Life Science Institute (The World Premier International Research Center Initiative), Kanazawa University, 920-1192, Japan.
[80]Graduate School of Life Science, University of Hyogo, Hyogo 678-1297, Japan.
[81]Institut de Physique du Globe de Paris, Université de Paris, Paris 75205, France.
[82]Department of Natural Sciences, International Christian University, Mitaka 181-8585, Japan.
[83]Institute of Geosciences, Friedrich-Schiller-Universität Jena, 07745 Jena, Germany.

[84]Center for Advanced Radiation Sources, The University of Chicago, Chicago, IL 60637, USA.
[85]SOLEIL Synchrotron, L'Orme des Merisiers, Gif sur Yvette Cedex, F-91192, France.
[86]Institut Chimie Physique, Université Paris-Saclay, CNRS, 91405 Orsay, France.
[87]Division of Mathematical and Material Science, Nagoya City University, Nagoya 467-8501, Japan.
[88] Department of Natural History Sciences, Hokkaido University, Sapporo 060-0810, Japan.
[89]Department of Earth and Planetary Sciences, Kyushu University, Fukuoka 819-0395, Japan.
[90]Graduate School of Advanced Science and Engineering, Hiroshima University, Higashi-Hiroshima 739-8526, Japan.
[91]Department of Geology, Rowan University, Glassboro NJ 08028, USA.
[92]Lunar and Planetary Laboratory, University of Arizona; Tucson AZ 85705, USA.
[93]Research and Development Directorate, JAXA, Sagamihara 252-5210, Japan.
[94]Department of Mechanical Engineering, Kanagawa Institute of Technology, Atsugi 243-0292, Japan.
[95]Marine Works Japan Ltd., Yokosuka 237-0063 Japan.
[96]Department of Science, Niigata University, Niigata 950-2181, Japan.
[97]National Astronomical Observatory of Japan, Mitaka 181-8588, Japan.
[98]Information Technology and Human Factors, National Institute of Advanced Industrial Science and Technology, Tokyo 135-0064, Japan.
[99]JAXA Space Exploration Center, JAXA, Sagamihara 252-5210, Japan.
[100]Department of Physics and Astronomy, Seoul National University, Seoul 08826, Korea.
[101]Department of Information Science, Kochi University, Kochi 780-8520, Japan
[102]Center for Data Science, Ehime University, Matsuyama 790-8577, Japan.
[103]Department of Earth and Environmental Sciences, Nagoya University, Nagoya 464-8601, Japan.

Abstract: Samples of the carbonaceous asteroid Ryugu were brought to Earth by the Hayabusa2 spacecraft. We analyzed seventeen Ryugu samples measuring 1-8 mm. There are CO_2-bearing water inclusions within a pyrrhotite crystal, indicating that Ryugu's parent asteroid formed in the outer Solar System. The samples contain objects formed at high temperatures such as chondrules and Ca, Al-rich inclusions with low abundances. The samples are rich in phyllosilicates and carbonates formed by aqueous alteration at low-temperature, high-pH, and water/rock ratios < 1 by mass. Less altered fragments with olivine, pyroxene, amorphous silicates, calcite, and phosphide are identified. Numerical simulations based on mineralogical and physical properties of the samples indicate that the Ryugu parent body formed at ~ 2 million year after the birth of the solar system.

Main Text

The carbonaceous asteroid (162173) Ryugu is a rubble pile formed by reaccumulation of material ejected from a parent asteroid by a large impact (*1*). Remote sensing observations have shown that Ryugu is related to hydrous carbonaceous chondrite meteorites (*2*). However, there are some differences with those meteorites, suggesting later heating and partial dehydration of Ryugu (*2*, *3*). Reflectance spectra are nearly uniform across Ryugu's surface, indicating minimal compositional diversity at its surface (*2*, *3*), except for some boulders (*3*, *4, 5*).

We expect samples of Ryugu to retain a record of the formation and early evolution of the parent body and Ryugu itself. We analyzed samples collected by the Hayabusa2 spacecraft *(6)*,

seeking to determine i) when and where in the solar nebula Ryugu's parent asteroid formed, ii) the initial mineralogy and water ice content, iii) how these original materials evolved through water-rock reactions, iv) how the asteroid was heated by the decay of short-lived radionuclides, and v) how the material was ejected from the parent body by an impact and re-accumulated to form Ryugu.

We analyzed seventeen Ryugu particles ranging from 1 to 8 mm in size (Fig. 1A shows the largest particle, C0002, and Fig. S1 shows all particles), consisting of six particles from chamber A, collected at the first touchdown site (TD1), and ten particles from chamber C, collected at the second touchdown site (TD2) (*6*). We refer to these mm-sized particles as coarse samples. Finer-grained powder samples (<1 mm in size: Fig. S2) obtained from TD1 and TD2 were also used for reflectance spectroscopy.

Reflectance spectra

Visible (Vis), near-infrared (NIR), and mid-infrared (MIR) [wavelength range (0.4 - 18 μm)] reflectance spectra were measured from many of the coarse Ryugu samples packed together (seven particles from TD1 and seven particles from TD2: Fig. S1), from the powder samples, and from samples of meteorites Orgueil and Tagish Lake, without exposure to air in entire analysis procedures ((*7*) and Fig. S2). MIR and far-infrared (FIR, 17-100 μm) reflectance spectra were also measured in air for sample A0026 and samples of the meteorites Orgueil, Alais, Tagish Lake, and Murchison.

All analyzed Ryugu samples exhibit similar Vis-NIR spectra (Fig. 2A). They have ~2.0-2.5% reflectance (at 550 nm) with a slightly red slope of ~0.1-0.3% μm^{-1} (0.48 to 0.86 μm) and ~0.2-0.3% μm^{-1} (2.0 to 2.5 μm). There are no strong absorption features blueward of 2.7 μm (Fig. 2A). No 0.7 μm absorption, due to Fe^{3+}-rich phyllosilicates (*8*), was detected. The Ryugu samples have an absorption band (~20% in depth) centered at ~2.71 μm (Fig. 2B), which is due to O-H stretching vibrations in Mg-rich phyllosilicates (*9*, *10*). A weaker absorption band at ~3.1 μm is possibly due to ammoniated salts or other nitrogen-bearing compounds (*11*). Absorptions at ~3.4–3.5 μm are due to aliphatic organics and carbonates, and those at ~3.8–3.95 μm are due to carbonates. In the MIR-FIR, the Christiansen feature, the reflectance minimum characteristic for the chemical composition, is present at ~9.1 μm. Reststrahlen bands, the reflectance peaks associated with Si-O stretching and bending modes, appear as strong peaks at ~9.8 μm, with a shoulder at ~10.75 μm, and as a doublet at ~22.3 μm (Fig. 2C).

Visible spectra of the touchdown sites were obtained by the Optical Navigation Camera Telescope (ONC-T) (*3*) on the Hayabusa2 spacecraft at spatial resolution of 0.3-0.5 m $pixel^{-1}$, before and after the sample collection. The location of TD1 showed higher reflectance than TD2 (Fig. 2D). We find similar results: the coarse and powder Ryugu samples from TD1 both exhibit higher reflectance than those from TD2 (Fig. 2A). The surface reflectance decreased after the touchdowns because the spacecraft thrusters removed powder from the surface of Ryugu during ascent (Fig. 2D) (*12*). Visible spectra of the coarse and powder Ryugu samples have similar reflectance values to the ONC-T spectra of the landing sites *(7)*, and to the global average (Fig.2A), indicating that the samples are representative of the global spectral properties of Ryugu. Reflectance ratios of ONC-T to the powder samples at 0.55μm is ~0.9 for both TD1 and TD2 (Fig. 2D).

Spectra of the Ryugu samples are generally consistent with Ryugu average spectra measured with Hayabusa2's ONC-T (*3*) and Near Infrared Spectrometer (NIRS3) (*2*) instruments. There are some differences between the NIRS3 and laboratory spectra (Fig.2A), even after converting both to the same wavelength resolution (Fig. 2B). The NIRS3 spectra have lower

reflectance R relative to sample (*R*NIRS3 *R*sample^{-1} = 0.7 at 2.0 μm) and a shallower 2.7 μm absorption depth *Depth* (*Depth* NIRS3 *Depth* sample^{-1} = ~0.5 at 2.7μm), consistent with (*13*)). This could be due to differences in particle size distribution and porosity between the laboratory samples and Ryugu's surface, or the much larger field of view of NIRS3 (see also (*13*)).

Ryugu and the laboratory samples have similar reflectance to asteroid Bennu (*14*) in the visible wavelength but opposite spectral slopes (Fig. 2A). The 2.7 μm feature (Fig.2B) and the bands in the MIR-FIR spectrum (Fig.2C) of Bennu (*15*) also differ from Ryugu.

The Ryugu samples are much darker and have a flatter spectral slope than the meteorites Orgueil and Tagish Lake (Fig 2A). Orgueil is classified as a CI1 meteorite, meaning an aqueously altered (modified by reactions with water) Ivuna-type carbonaceous chondrite, while Tagish Lake is a C2, a carbonaceous chondrite that was less altered so retains anhydrous minerals. The position of the OH absorption band in the Ryugu sample spectra is consistent with that in Orgueil, Tagish Lake, and the ungrouped C1 chondrite Flensburg in which sub-millimeter size anhydrous aggregates made of silicate and glass, chondrules, are totally replaced by phyllosilicates (*16*). The same feature appears at longer wavelengths in the Murchison CM2, carbonaceous chondrite meteorites of Mighei type, and asteroid Bennu (Fig. 2B; (*2*, *14*)). The position of this band is known to correlates with Mg/Fe ratio in phyllosilicates, so we infer that Ryugu, Orgueil, Tagish Lake, and Flensburg contain Mg-rich phyllosilicates, while Murchison and Bennu contain Fe-rich phyllosilicates (*9*, *10*).

3D structure and density

All our coarse Ryugu samples, except one sample A0058, were characterized using synchrotron X-ray computed tomography (SR-CT (*7*)), with a resolution of 0.85 micron/voxel (Table S1). Most of the samples had an irregular shape, but some exhibited one or two broad flat surfaces. Particles with flat surfaces were also observed during the sample collection process (*6*). The particle interiors have cracks; most are irregular, but some particles (e.g., C0055) contain parallel cracks with spacings of tens to hundreds of microns (Fig. S3).

The mass of each coarse sample particle was measured under dry conditions in a glove box and the density was calculated from the sample volume determined using SR-CT (Table S1). The bulk density (mass/total volume, including cracks and pores) ranged from 1.7 to 1.9 g/cm^3 with an average of 1.79±0.08 g/cm^3 (Table S1), which is higher than estimated from earlier measurements in the curation facility (1.3 g/cm^3 (*17*)) which did not consider the full 3D structure. These densities are higher than the measured average density of Ryugu (1.2 g/cm^3: (*1*)), indicating that the asteroid has high internal macro-porosity. The average bulk densities of CI (Ivuna-type) and CM (Mighei-type) chondrite meteorites are 2.12 and 2.21g/cm^3, respectively (*18*), while the ungrouped C1 chondrite Flensburg has density 1.98 g/cm^3 (*16*). Considering mineralogical similarities to CI chondrites, the lower density of Ryugu samples indicates higher porosity of Ryugu samples than CI chondrites.

Mechanical, thermal, electrical, and magnetic properties

The Ryugu samples A0026 (TD1) and C0002 (TD2, our largest particle) were measured (*7*) to determine mechanical, thermal, electrical, and magnetic properties (Tables 1) to compare with carbonaceous chondrites (Table S2) and for use in numerical simulations.

The resulting physical properties of the Ryugu samples are not identical to any known meteorite. Most properties are similar to hydrous CI and CM chondrites, but differ from anhydrous CV (Vigarano-type) and CO (Ornans-type) chondrites (Tables 1 and S2). The mechanical properties show that Ryugu samples are weaker in strength, especially Young's

modulus and Poisson's ratio, than hydrous carbonaceous chondrites (Table S2) and have a larger volume change upon deformation (such as compression or impact). The thermal expansivity of the Ryugu samples differ from the nonlinear temperature-dependent results measured for some carbonaceous chondrites (*19*), but is linear in the temperature range of 220-370 K (Fig. S4).

The thermal properties (Table 1) could be responsible for the low thermal inertia of Ryugu (*20*, *21*). The thermal diffusivity (Table 1) and the bulk density of sample C0002 (Table S1) were used to calculate the thermal conductivity of 0.5 $Wm^{-1}K^{-1}$ and thermal inertia of 890 J m^{-2} $s^{-0.5}$ K^{-1} (hereafter thermal inertia units, TIU) at a temperature of 298 K. The thermal inertia of the sample is higher than the mean of the asteroid surface observed by Hayabusa2 [225 ± 45 TIU (*22*)], and measured in situ at the Mobile Asteroid Surface Scout (MASCOT) landing site [295 ± 18 TIU (*21*)]. Remote sensing is sensitive to a thermal skin depth of ~10 mm, whereas the thickness of the sample measured in the laboratory is <1 mm, so a thermal shielding effect could arise on intermediate scales (e.g. cracks of several millimeters length).

Thin sections of magnetite framboids (aggregates of equidimensional microcrystals of magnetite) with diameters of 300-1100 nm were observed using electron holography at a spatial resolution of 14 nm (*7*). These magnetite inclusions have vortex magnetic structures and magnetic flux leakage out of the particles (Fig. 3A-C, and S5). The externally leaking magnetic flux was detected as remanent magnetization in macroscopic measurements. Mössbauer spectra showed that half of the iron in these samples is in magnetite, and the magnetic hysteresis parameter values (Table. 1) were consistent with the submicron-sized equidimensional magnetite framboids (*24*, *25*). Therefore, the magnetite framboids dominate the natural remanent magnetization (NRM) of asteroid Ryugu. Two Ryugu particles from different sampling sites (A0026 from TD1 and C0002 from TD2) record magnetic fields of 31–260 μT and 18-704 μT (Fig. S6), respectively.

Elemental abundances

We used muon X-ray emission spectroscopy to measure the abundances of major chemical elements in the ten coarse Ryugu samples, including the largest sample C0002 (126.6 mg in total) (*7*, *25*, *26*). Because the muon beam is > 3cm in diameter, we analyzed all ten samples together to obtain a mean bulk elemental abundance. Pellets of the meteorites Murray (CM2; 306.5mg) and Orgueil (CI1; 195mg) were measured for comparison.

We detect carbon, nitrogen, oxygen, sodium, magnesium, silicon, sulfur, iron, and nickel (Figure 4A). The Ryugu and Orgueil spectra are very similar, indicating similar major elemental abundances. However, the Ryugu samples contain less oxygen than Orgueil.

We calculated elemental mass ratios *M*/Si (*M*=C, N, O, Na, Mg, S, and Fe) from the muon X-ray data (*7*). *M*/Si has previously been measured for the Murray meteorite (Table 3), so it was used as a standard. We determined Ryugu mass ratios of C/Si=0.338±0.008, N/Si=0.019±0.009, O/Si=3.152±0.099, Na/Si=0.039±0.006, Mg/Si=0.890±0.021, S/Si=0.510±0.019, and Fe/Si=1.620±0.040. These elemental ratios are consistent with CI chondrites (*27*) and the Sun *(28*), except O/Si is 25% lower in Ryugu than CIs (Table S3 and Fig. S7). These abundances nevertheless classify Ryugu as a CI chondrite, consistent with other lines of evidence *(29)*.

CI chondrites contain 45 wt% oxygen (*27*); Ryugu is depleted in oxygen by 11.3 wt%, given its similar Si concentration to CI chondrites (*29*). The Ryugu samples were prepared and analyzed in low oxygen conditions (< 0.1%) and in dry atmosphere (dew points < -50°C), so the

indigenous oxygen abundance of Ryugu samples was determined. The lower water content and sulfate abundance of Ryugu samples than CI chondrites (*29*) is probably the cause of the low oxygen abundance.

Nitrogen-bearing molecules, such as NH_3, CN, and N_2, have low freezing points and could only have been incorporated into asteroids in the outer Solar System (*30*). The N/C ratio can therefore be used to infer the distance from the Sun of Ryugu's parent body during its formation. We measured an average N/C atomic ratio of 0.047±0.022 from the ten coarse samples. This is higher than primitive anhydrous chondrites (N/C = 0.001 to 0.02), consistent with hydrated chondrites such CM and CI (N/C = 0.02 to 0.06), and lower than ultra-carbonaceous micrometeorites of probable cometary origin (N/C = 0.06 to 0.2) (*30*). We conclude that Ryugu's parent body formed at heliocentric distances similar to hydrated carbonaceous chondrites.

Mineralogy and mineral chemistry

The SR-CT image of C0002 (Fig. 1B) shows that it consists almost entirely of fine-grained matrix material. No distinct objects formed at high temperatures (>1000 °C) in the early solar nebula such as chondrules (formed by melting of precursor silicate-rich dust) or Ca, Al-rich inclusions (CAIs: formed by condensation from hot nebular gas and the earliest material in the solar system) over 100 μm were found from all coarse samples, but there are smaller examples (discussed below).

We produced 31 polished sections cut from 11 samples (Table S4) including 2 plates from the largest sample C0002. Observations with field-emission electron microscopes show that most of the coarse samples are breccias consisting of fragments ranging in size from ~10 to ~500 microns. Elemental abundance maps of Na and Mg show compositional differences between fragments (Fig. S8), usually with sharp boundaries. Most of the fragments consist primarily of fine-grained matrix material, with similar (though not identical) mineralogy and mineral chemistry, which we refer to as Ryugu's major lithology. CI1 chondrites have similar properties, with Orgueil being the most brecciated, with the Ryugu samples having similar brecciation to Orgueil *(31, 32)*.

The major lithology of Ryugu (Fig. 1C) consists of minerals formed by aqueous alteration: the dominant phase is a phyllosilicate-rich matrix that contains minerals including abundant iron sulfides (pyrrhotite and pentlandite), carbonates (breunnerite and dolomite), magnetite, and hydroxyapatite. The phyllosilicates consist of the minerals saponite and serpentine. Chlorite was only detected in a limited area in C0076. Mg-Na phosphate occurs in some places and appears to have shrunk in volume since its formation, probably due to degassing of volatile species, such as water (Fig. S9). Dolomite is the most abundant carbonate mineral; breunnerite is less abundant but occurs as larger crystals, with one in C0002 measuring 940μm × 450μm × 262 μm (Movie S1). Ca carbonate is rare. Pyrrhotite crystals with a pseudohexagonal shape (1-100 μm) are abundant and sometimes include pentlandite. Nano- to submicron-size pyrrhotite and pentlandite crystals occur ubiquitously in the phyllosilicate matrix (Fig. S10). Magnetite is present in diverse morphologies (Fig. S11), which is typical of CI1 chondrites (*19*). The carbonates often contain small (< 10 μm) crystals of magnetite and pyrrhotite. Small (< 10 μm) olivine and low-Ca pyroxene crystals are present but rare; they are completely absent from some of the coarse samples.

Ferrihydrite was not observed, despite being a major component of Orgueil (*33*, *34*). Nor was magnesium sulfate. Calcium sulfate (gypsum; $CaSO_4(H_2O)_2$) was detected only as very

small grains around larger crystals of calcite (Fig. S12) and probably formed after sample recovery on Earth, by reactions of calcite with sulfuric acid that is produced by oxidation of small pyrrhotite crystals within Ryugu samples *(35, 36)*. Small crystals of sodium sulfate grow on the surface of polished sections of Ryugu samples (Fig. S13), which is apparently terrestrial origin. We infer that sulfates are likely absent on Ryugu, implying that sulfates in CI1 chondrites are terrestrial contamination (*37*). Additional minor minerals include chromite, Mn-rich ilmenite, spinel, ZnS, cubanite, and daubréelite. Carbonaceous material occurs as globules and diffuse objects in matrix.

Phyllosilicates in the major lithology have Mg# (defined as atomic ratio of Mg/(Mg+Fe)× 100) mostly in the range of 75-90, similar to Orgueil, but Ryugu phyllosilicates have more magnesium-rich varieties than in Orgueil, because Ryugu data are plotted in the Mg#>85 area (Fig. 4B). The compositions of the carbonates are very similar to CI1 chondrites (Fig. 4C). Breunnerite and dolomite contain 1-10 and 2-5 wt % MnO, respectively. Hydroxyapatite contains a small amount of fluorine (< 1 wt%), typical of chondrites (*38*). We performed high-energy synchrotron X-ray fluorescence (XRF) tomographic analysis (*39*), finding enrichment of rare-earth elements (REEs) in hydroxyapatite, with mutually-consistent levels of each REE (Fig. S13). This is unlike apatite grains in ordinary chondrites (*40*) and Orgueil (*32*), which have higher levels of Eu and Gd, respectively, than other REEs. Ordinary chondrites and CK (Karoonda-type carbonaceous chondrites) have REE abundances that decrease from light to heavy atomics masses (*40*), unlike Ryugu. The magnetite does not contain detectable trace elements, while ilmenite contains various concentrations of MnO up to 10 wt%, both typical of CIs (*34*, *41*). Pyrrhotite contains Ni up to 2 wt%. The Ni/Fe atomic ratio of pentlandite ranges from 1 to 1.2 in most cases. Representative compositions are listed in Table S5.

Relative mineral abundances were estimated from two element maps of C0002 (~9.0 and ~8.6 mm^2 area) composed primarily of the major lithology. The abundances (Table S6) are broadly consistent with those of Orgueil (*31*, *32*, *42*).

We performed X-ray diffraction (XRD) analysis of a whole sample of C0002 (Fig. S15), finding a large, broad peak at approximately 10 Å and a distinct peak at 7.45 Å, which we identify as due to saponite and serpentine, respectively. The 10 Å peak indicates a low abundance of interlayer H_2O in saponite, as previously inferred using other techniques (*29*). To characterize the phyllosilicates, we applied ethylene glycol to 10 small particles separated from several coarse samples and observed peak shifts in the XRD patterns, indicating expansion of interlayer spacings due to addition of glycol (Fig. S16). We identify reflections at 16.8, 13.3 and 7.28 Å as due to saponite-serpentine mixed-layer minerals based on the first two reflections and pure serpentine from the last reflection *(7)*. The saponite-rich mixed-layer mineral is the most abundant followed by serpentine, but the relative abundances differ between samples. Similar results have previously been obtained for Orgueil (*43*).

Although the bulk mineralogy of Ryugu samples is similar to Orgueil, we found above that the Ryugu samples are much darker. Possible explanations are the presence of bright Mg-sulfate epsomite in Orgueil *(37)*, and a lower Fe^{3+} abundance in phyllosilicates in the Ryugu samples (Fe^{3+}/Fe_{total} is 0.4 for Ryugu and 0.9 for Orgueil). Mg-rich smectite becomes brighter as Fe^{3+}/Fe_{total} increases from 0.40 to 0.97 (*44*). The oxidation of phyllosilicates and the formation of epsomite can occur on Earth due to weathering, which we infer is the likely origin of the brightness of Orgueil. Ryugu samples also contain a high abundance of opaque, nano-size pyrrhotite, (Fig. S10) which acts as a darkening agent; Orgueil lacks these *(34)*, possibly also due to oxidation on Earth (*45*).

The mineralogy, mineral chemistry, and relative mineral abundances of the major

lithology indicate that Ryugu (or its parent body) experienced pervasive aqueous alteration. Except for the lack of sulfate and ferrihydrite, the petrological and mineralogical properties of Ryugu are consistent with the five CI chondrites (*31*, *32, 34, 46–48)*; we therefore classify the Ryugu samples as CI chondrites.

Less altered fragments

While most Ryugu fragments have experienced extensive aqueous alteration, some fragments in samples of C0002, C0033, C0023, C0025, C0040, C0046, C0076, and C0103 show a considerably lesser degrees of alteration. Electron-microprobe analysis *(7)* indicates that these fragments contain higher abundances of olivine and pyroxene (Table S6). Electron diffraction (Fig. S17) shows that they also contain calcite or aragonite (not dolomite or breunnerite) and phosphides (schreibersite $(Fe, Ni)_3P$ and allabogdanite $(Fe, Ni)_2P$) not hydroxyapatite. These are characteristic features of a less-altered lithology. These less-altered fragments are enriched in Na, with Na/Si ratios ~2 times that of the Sun (Table S7).

We identified five less altered fragments in one of the thin sections of C0002. The Mg map of C0002 (fragment 1 in Fig. S8B) indicates a high abundance of olivine and low-Ca pyroxene, which are rich in Mg relative to surrounding phyllosilicates, and spinel grains with sizes < 30 μm (Fig. S18 and Table S6). Most olivine in the Ryugu samples occurs in these less altered fragments; it has Mg# > 97 (corresponding to FeO < 3 wt% in Fig. 4D), similar to olivine in CI chondrites (*49–51*). A similar, but more altered, fragment has previously been reported in Orgueil [(*52*), their clast 1].

We identified the two fragments that exhibit the least alteration among our samples: labelled fragments 4 and 5 in Fig. S8B. The fragments are small (Fig. S19: 130 μm x 50 μm and 200 μm x 90 μm for fragment 4 and 5, respectively) and embedded within the major lithology. They have a very porous texture, dominated by submicron particles of olivine, pyroxene, and other smaller silicate phases with numerous iron sulfide inclusions (Fig. 3D and E). They also contain micron-sized regions of Ca carbonate, pyrrhotite, Al spinel, magnetite spherules, small quantities of phosphides, MgNa phosphate, pentlandite, Cr spinel, and tochilinite, a hydrous sulfide that is abundant in CM2 chondrites (*53*) (Fig. S20). These mineral assemblages are similar to fragment 1, but the abundance of olivine and pyroxene is much higher (12.8 and 14.1 vol % for olivine in fragments 4 and 5, respectively; see Table S6). Most of the olivine and pyroxene is enriched in Mg, but examples of Fe-rich olivine (Mg#<44) are also present. Several small areas in fragment 4 contain Na-rich phyllosilicate, indicating that aqueous alteration fluids were enriched in sodium. The high abundance of anhydrous silicates leads us to classify the least altered fragments as CI2 (a CI chondrite that was altered but still retains anhydrous minerals), rather than CI1 (in which almost all anhydrous silicates are replaced by phyllosilicates).

We observed the least-altered fragments using transmission electron microscopy (TEM *(7)*), finding that the least-altered fragments also contain numerous partially rounded, mostly 100-500 nm, amorphous silicate objects that contain abundant Fe sulfides (mainly < 50nm pyrrhotite and minor pentlandite) (Fig. 3F and S21A). These objects are similar in texture and composition (Fig. S21A and B) to glass with embedded metal and sulfides (GEMS) that occur in anhydrous chondritic interplanetary dust particles (IDPs) of probable cometary origin (*54*). The silicates are mostly amorphous or very poorly crystalline material (the latter possibly phyllosilicates) with lattice spacings close to 2.6 and 1.5 Å (Fig. S21A). This is similar to fine-grained fibrous material reported in the GEMS-like objects in the Paris CM chondrite (*56*).

However, there are differences between the least-altered Ryugu fragments and GEMS in IDPs. The GEMS-like objects we identify in Ryugu lack Fe metal, instead containing pyrrhotite,

pentlandite and tochilinite. The silicates have signs of incipient alteration to phyllosilicates (Fig. S21A). The Mg-rich silicate composition of the GEMS-like objects in Ryugu is similar to the silicates in GEMS in IDPs (Fig. S21B), but also to the phyllosilicate composition in the major lithology (Fig.4B). This indicates that the GEMS-like objects in Ryugu are at least partially altered, similar to the primitive clasts in the Paris CM chondrite (*56*, *57*).

Chondrules, CAIs, and porous olivine

We do not identify any normal sized chondrules (100-1000 μm) in the Ryugu samples analyzed using SR-CT. However, some smaller objects and fragments (Fig. 3G-I) have features characteristic of chondrules. Some of these (Fig. 3G and 3H) contain FeNi metal spheres embedded in Mg-rich olivine (Mg#>98), indicative of melting in very chemically reduced conditions, which is typical of type-I chondrules that consists mainly of olivine with Mg#>90. One object has a barred olivine texture in TEM observations (Fig. 3I) - a thin rim and many bars constituting a single crystal of Mg-rich olivine. Therefore, this object is a type-I barred olivine chondrule. No glass is present between the olivine bars, only pores, probably indicating glass was originally present but dissolved during the early stages of aqueous alteration. We also identified a small (~ 30 μm in size) chondrule that has been completely replaced by phyllosilicates (Fig. S22 and Movie S2). Similar completely altered chondrules have previously been found in the ungrouped C1 chondrite Flensburg, although they are larger (>300 μm) (*16*). The small size and low abundance of the chondrules in Ryugu are similar to those found in samples of the short-period comet 81P/Wild2 (*58*).

We also identified a few small (< 30 μm) CAIs in the Ryugu samples (Fig. 3Kand L). Their sizes are smaller than CAIs in the Ivuna CI1 chondrite (~100 μm) (*59*). One of the CAIs (Fig. 3K) consists of half hibonite and half Al-rich Fe-free spinel, with a small perovskite inclusion. Another (Fig. 3L) consists solely of Al-rich Fe-free spinel, with a small hibonite and a perovskite inclusion. We interpret this as evidence that CAI material that is susceptible to aqueous alteration, such as melilite (*60*), was replaced by phyllosilicates. Several CAI-related spinel-rich aggregates, together with forsteritic olivine, were also observed (Fig. S18).

Forsterite (Mg#98-99) grains occur in the less-altered lithology, being < 30 μm in size with numerous micron-size pores. One (Fig. 3J) contains Al, Ti-bearing Ca, Mg-rich pyroxene, diopside. We analyzed 20 grains porous forsterite by an electron microprobe, finding they all contain ~0.5 wt% MnO. Atomic ratios of Mn/Fe do not exceed 1 in most cases and thus they are not low-iron manganese-enriched (LIME) olivine (*61*). The pores suggest partial dissolution during aqueous alteration. The origin of this porous olivine is unclear; they could be condensation products, similar to amoeboid olivine aggregates (AOAs) found in carbonaceous chondrites (*62*), although the texture of the olivine crystals in Ryugu is different from AOAs (*63*).

Fluid inclusion in pyrrhotite

We performed higher resolution (~50nm/voxel) synchrotron nano-computed tomography (SR-nanoCT) of a large pyrrhotite crystal taken from sample C0002. This showed probable fluid inclusions in the center (Fig. 5A, B), suggesting the fluids were trapped in the early stages of crystal growth. These inclusions are completely encapsuled in pyrrhotite and filled with a homogeneous light-element material (Fig. S23). We performed Time-of Flight-Secondary Ion Mass Spectrometry (TOF-SIMS) depth profiling and lateral mapping (<80 nm/pixel) at a temperature of -120°C to expose and measure, respectively, the composition of the (now frozen) fluids in five inclusions.

The TOF-SIMS measurements show that the trapped fluids were solutions containing H_2O, CO_2, sulfur species, and nitrogen- and chlorine-bearing organic compounds. These were identified by their representative secondary ion species including O^-, OH^-, CO^-, C_2^-, C_2H^-, Cl^-, S^-, and CN^- (Fig. 5C). The detection of CO^-, C_2^-, C_2H^- and C_3^- suggests a complex molecular structure of organic molecules dissolved in the aqueous solution. Electron microscope observation of the largest inclusion show no phyllosilicates or other OH^- bearing phases that could have contributed to the signal (Fig. 5D). The presence of CO_2-bearing water in a crystal of pyrrhotite indicates that the Ryugu parent body formed beyond the snow lines, boundaries between gas and ice, of H_2O and CO_2 in the early Solar System, i.e. > 3-4 astronomical units (au) from the Sun (*64*).

Flat surfaces and CuS table coral-shaped object

We identified some features of the Ryugu samples that have not been observed in meteorites. These include very flat surfaces of coarse samples (Fig. 6A). We cut five slices (each 10 × 10 × 0.1 μm) from the flat surface of A0067 to perform depth profiles. TEM observations show a 2 μm thick saponite-rich layer with high Mg#~90 running along the flat surface (Fig. 6B). The saponite layer is superposed on an irregular surface of the major lithology, indicating that it formed later. All five slices show similar features, which we infer are present across the whole flat surface. The formation of saponite layer requires fluids were present. Pyrrhotite crystals on the flat surface are aligned with their pseudohexagonal facets parallel to the saponite layer (Fig. S24), implying a compressive force during formation. One possible explanation is ice lensing, formation and growth of lens-shaped ice (*65*, *66*), as occurs in permafrost soils. At the final stage of aqueous alteration, fluids could have been segregated in thin cracks as they froze. Ice in the cracks would then have grown to form ice lenses. The pressure exerted by the expanding ice lens would have squeezed the adjacent regolith, compacting and aligning phyllosilicates, especially expandable clays such as saponite (*66*).

We also identified table coral-shaped growths of a CuS phase on the flat surface of A0067 (Fig. 6C). A thin section was made by cutting the CuS object perpendicular to the flat surface, then observed with TEM. The CuS has a morphology which resembles a table coral, with a root, several branches, and many disk-shape crystals on top (Fig. 6D). Electron diffraction suggests that the CuS phase is probably digenite (Cu_9S_5), which is of hydrothermal origin (*67*). We cannot determine the formation mechanism, but it might have grown from a solution that filled a crack exposed on the flat surface.

Shock effects

Most of our samples show no features indicating strong deformation or shock melting, indicating the collected material generally did not experience any intense shock. However, C0055 shows evidence of uniaxial compression and sets of parallel fractures perpendicular to the compaction axis (Fig. S3). Such features are common in shocked hydrous carbonaceous chondrites (*68*) and appear in experiments that shocked the Murchison CM2 chondrite to a pressure of 20 GPa (*69*). Therefore, C0055 experienced a shock and other 16 samples seem to free of shock effects.

Aqueous alteration conditions

The low abundance of Mg-chlorite suggests that aqueous alteration occurred at low temperature, below the ~ 100 °C (*70*) required to stabilize Mg-chlorite . The monoclinic 4C

structure, one of crystal structures of pyrrhotite having three unequal crystal axes with one oblique intersection, of all 10 pyrrhotite crystals observed with X-ray and electron diffraction indicates they formed below 254 °C (*71*). The Ryugu pentlandite and pyrrhotite compositions are most consistent with 25°C (Fig. S25) [(*67*), see also (*72*, *73*)], suggesting low-temperature formation. The site occupancy by Fe and Ni in pentlandite and its lattice constants are a function of temperature (*74*). We measured the pentlandite lattice constant of 10.0643±0.0009 Å using XRD analysis of a single pentlandite crystal, 5 μm in size, which was separated from sample C0040, following established methods (*75*). This lattice spacing, and the chemical composition, indicate an equilibrium temperature of 20 ± 29.5°C (Table S9). O isotopes in dolomite indicate formation at 37±10 °C (*29*). All these temperature estimates are consistent.

Mössbauer spectra (conventional and synchrotron) were collected from 1-mm size fragments taken from C0061 and A0026 in N_2 conditions. These show that magnetite is not oxidized (Table S9). The Fe^{2+}/Fe_{total} ratios measured from the phyllosilicates are approximately 0.61 for C0064 and 0.48 for A0026 (Fig. S26). Magnetite, pyrrhotite, and silicates contain 40 to 50, 15 to 30, and 25 to 40 % total iron, respectively (by atom, Table S9). Micro-X-ray Fluorescence X-ray absorption near edge structure (μ-XRF XANES) analysis of the Fe K-edge, a sudden increase of X-ray absorption just beyond the binding energy of the K-shell electrons of Fe atom, using a 1.0 μm × 1.0 μm X-ray beam (*76*) was performed in N_2 condition using a 150-μm sized particle separated from sample C0025. The Fe^{2+}/Fe_{total} ratio in phyllosilicates was determined to be 0.6 to 0.7 (Fig. S27), consistent with the Mössbauer data.

The determination of Fe^{2+}/Fe_{total} ratio in other minerals, specifically saponite and serpentine, is required to determine the redox conditions during formation, because the stability of Fe^{2+} in each phase can be different. We used scanning transmission X-ray microscopy (STXM; (*77*)) analysis with a ~50 nm spatial resolution to measure Fe^{2+}/Fe_{total} in the saponite layers in A0067 (Fig. 6B), finding 0. 68±0.05 (Fig. 4E and 4F). The sample must have been oxidized to some degree during its storage in a desiccator for more than five months, so we regard this ratio as a lower limit. Based on (i) the relationship between Fe^{2+}/Fe_{total} ratio and oxidation reduction potential E_h determined for the minerals nontronite and high Fe-bearing montmorillonite (*78*); and (ii) a reduction experiment we performed on terrestrial saponite with Fe^{2+}/ Fe^{3+} ratio determined by XANES (Fig. S28); we infer that the Fe^{2+}/Fe_{total} (> 0.68) obtained from A0067 indicates that the Eh of saponite formation was likely lower than -0.45 V. If we assume that the this Eh value is valid at neutral to alkaline pH conditions, and combine it with other μ-XRF-XANES data on a dominant oxidized arsenic form (As^{3+}) in As-bearing species in A0067 (Fig. S29), we infer fluid pH > ~9 based on the Eh-pH diagram of As compounds at 25°C (*79*). The presence of saponite on Ryugu also indicates an alkaline fluid (pH > 8) based on (i) the stability field of saponite in the Eh-pH diagram of Fe and (ii) the pH condition of terrestrial lakes where saponite has been found (*80*).

We conclude that aqueous alteration proceeded at ~25°C in alkaline conditions.

Chemical equilibrium modeling of aqueous alteration

Aqueous alteration cannot have begun until accreted ices melted in the interior of Ryugu's parent body, and likely continued until temperatures reached ~40 ºC (this study and (*29*)). We therefore performed chemical equilibrium modeling of a water-gas-solid system at 0-40 ºC (*7*). Consistent with the muon analysis (Table S3), we assumed the initial accreted rock had the elemental composition of CI chondrites, but with additional H, C, O, S and Cl. Our model mixes this rock in different proportions with a water-ice rich component, which contains CO_2 and HCl, reflecting the presence of CO_2 and Cl in the fluid inclusion (Fig. 5) and the

inferred C and Cl sources in carbonaceous chondrites (*81*, *82*). Although Ryugu material may not have reached chemical equilibrium during alteration, we run our calculations to that stage.

Figure 7A-D show our calculated equilibrium composition of the water-gas-solid system at 40 ºC, as a function of the initial melted ice/rock and the water/rock (*W*/*R*) mass ratio. Only 10% of organic matter is allowed to react *(7)*. The modeled mineralogy (Fig. 7A) at initial *W*/*R* of 0.06 to 0.1 reproduces the least-altered lithology we found in the Ryugu samples (Table S6). These and lower *W*/*R* ratios permit stable reduced phases (e.g. Fe-rich metal, phosphides), which could remain unaltered or form through alteration under water-poor and H_2-rich conditions. A higher *W*/*R* ratio of 0.1 to 0.2 matches the less-altered lithology, and *W*/*R* of 0.2 to 0.9 with pH > 9 (Fig. 7C) matches with the more extensively altered major lithology (Table S6). Different calculations are performed at temperatures below 40 ºC (0 ºC and 20 ºC) and the results are similar to those at 40 ºC *(7)*.

Our calculations show high Na concentrations at lower *W*/*R*, both in the fluid and in saponite (Fig. 7A, B), which are consistent with the Na-rich composition of the least- and less-altered lithologies of Ryugu (Table S7). The modeling indicates an initial Mg-Na-Cl solution with H_2O-CO_2 in the gas phase, which evolved towards a more reduced and Na-Cl alkaline brine that coexisted with a H_2-rich gas phase (Fig. 7B-D). No sulfates form in the model, due to the reduced conditions, which is consistent with our observation of the Ryugu samples. The formation of sulfates requires strong oxidants, such as H_2O_2 and H_2SO_4, in ices accreted on asteroids (*83*).

Formation of Ryugu's parent asteroid

The asteroid Ryugu was formed in a different orbit than its current near-Earth one. Orbital dynamics calculations have shown that the most likely origin is two asteroid families (Eulalia or Polana C) in the inner main asteroid belt (*3*, *4*, *84*, *85*). Our observation of CO_2-bearing aqueous fluid in Ryugu pyrrhotite is consistent with the parent asteroid having formed beyond the H_2O and CO_2 snow lines of the early Solar System, i.e. > 3-4 au from the Sun. This must have been followed by scattering inward, to the current orbit of the Polana and Eulalia families (< 2.5 au). We found many similarities between the Ryugu samples and CI chondrites, which suggests that CI chondrites might have a similar origin.

The Ryugu samples record a magnetic field (Fig. S6), which could have arisen from the nebular magnetic field, or the dynamo fields generated by differentiated objects (such as Jupiter). The homogeneous global reflectance spectra of Ryugu indicate its parent body was not differentiated (*2*, *3*). The stable component of NRM is likely carried by the framboidal magnetite (Fig. 3A-C). If the source was the nebular field (*86*), then the solar nebula had not yet dispersed when magnetite formed on Ryugu's parent body.

Our interpretation that Ryugu's parent asteroid formed far from the Sun is supported by the rarity and very small size of chondrules and CAIs in the samples (Fig. 3G-L), which are similar to those observed in comets *(58)*, the high abundance of carbonate (Table S6), and the presence of GEMS-like objects (Fig. 3F). However, the C/Si abundance ratio is not as high as those of comets (Table S3), based on measurements of cometary IDPs and ultra-carbonaceous micrometeorites (*30*, *87*, *88*). This indicates the parent body of Ryugu did not originate from comets themselves, but formed in the same region as CI chondrites, at a large heliocentric distance, possibly outside the orbit of Jupiter (*89*).

Thermal model of Ryugu's parent asteroid

We used the physical properties obtained from the sample analysis (Table 1) to calculate a thermal model of Ryugu's parent body. The radius of the parent body was chosen based on an estimate of the total mass of the Eulalia family (*85*). We set a radius of 50 km for the rocky part of the parent body, then added additional size according to the amount of water ice in each model. The initial internal and surface temperatures were set to – 200ºC (70K, see rationale (*7*)). The temperature was then allowed to increase due to heating by radioactive decay of ^{26}Al, which melts the water ice at 0 ºC. Subsequent formation of hydrous minerals (assumed to occur at 20 ºC) releases energy that causes further heating. We ran simulations for ranges of formation age (t_s) and initial *W*/*R* ratio.

Mn-Cr dating of Ryugu samples has indicated that carbonates formed at 37±10°C, 5.2 Myr after the formation of the first solid materials in the solar system (i.e., CAIs) (*29*). That temperature is consistent with our mineralogical constraints (mostly $\lesssim$ 50°C). Our chemical modeling of the aqueous alteration found that a *W*/*R* ratio of 0.2-0.9 reproduces the mineralogy of the major lithology (Fig. 7A). An example thermal model that satisfies these constraints (t_s ~2.2 Myr and *W*/*R* = 0.6) is shown in Figure 7E. Inside the parent body (~ 51 km radius from the center), ice melts, hydrous minerals form, and carbonate minerals precipitate at ~4.8 Myr. While hydrous and carbonate minerals form throughout, the subsequent temperature increase is limited (reaching a peak of ~75ºC), and therefore dehydration of the hydrous minerals does not occur. Within 14 km of the cold surface, ice melting is limited, so the initial mineralogy experiences very little alteration at low *W*/*R* ratios and low temperature (~0°C). Therefore, the least-altered lithology (Fig. 3D-F) we found in the Ryugu samples might have been located close to the surface of Ryugu's parent body.

The formation age in the model required to satisfy the constraints from the sample analysis varies depending on the initial *W*/*R*. The major lithology is consistent with *W*/*R*=0.2 to 0.9 (Fig. 7A), which corresponds to a range of formation ages from 1.8 Myr (*W*/*R*=0.9) to 2.9 Myr (*W*/*R*=0.2) after CAI formation (see Fig. S30). We assume instantaneous accretion of the parent body at the time of formation. On the other hand, if we assume slow accretion of the parent body, then the formation would have started earlier.

Catastrophic collision of Ryugu's parent body

Ryugu's parent body was disrupted by a large-scale impact to form the Eulalia or Polana asteroid family, including Ryugu itself (*3*, *90*). Using the physical properties measured from the samples (Table 1), we constructed an equation of state consistent with the Ryugu material and used it to calculate a destructive collision with the parent body (*7*) using the impact-Simplified Arbitrary Lagrangian Eulerian (iSALE) software (*91–93*). Figure 7F shows the head-on collision of a 6 km-radius impactor onto a 50-km-radius parent body at an impact speed of 5 km/s, typical for the main asteroid belt (*94*). In this simulation, the parent body is largely destroyed, with the diameter (*D*) of the largest surviving body being ~ 50 km (Fig. S31). This is consistent with the measured sizes of Eulalia (*D* = 40 km) or Polana (*D* = 55 km) (*85*).

Figure 7F indicates that, during the impact disruption of the parent body, regions that experienced high shock pressure and temperature are limited in volume. 10 and 0.2 volume % of the parent body experienced pressure higher than 1 and 10 GPa, respectively. The temperature near the impact site (approximated as the size of the impactor) rises above 700ºC, while regions away from the impact site do not rise above 90ºC. The latter temperature is consistent with the amount of interlayer water found in Ryugu saponite (*29*). With this temperature limitation and

the absence of evidence for shocks in most of our samples, we propose that Ryugu might have formed from fragments excavated from areas far from the impact site, such as on the far side. It is likely that some of the reaccumulated material originated from the surface and sub-surface layer of the parent body; such material would have experienced limited degrees of aqueous alteration at low temperature and low *W/R* ratio, consistent with the least-altered and the less-altered fragments found in our samples.

We conclude that the samples collected by the Hayabusa2 mission originating from multiple depths within Ryugu's parent body, which formed beyond the H_2O and CO_2 snow lines, possibly beyond the orbit of Jupiter.

References and Notes

1. S. Watanabe et al., Hayabusa2 arrives at the carbonaceous asteroid 162173 Ryugu-A spinning top-shaped rubble pile. *Science* **364**, 268–272 (2019). doi:10.1126/science.aav8032
2. K. Kitazato et al., The surface composition of asteroid 162173 Ryugu from Hayabusa2 near-infrared spectroscopy. *Science* **364**, 272–275 (2019). doi:10.1126/science.aav7432
3. S. Sugita et al, The geomorphology, color, and thermal properties of Ryugu: Implications for parent-body processes. *Science* **364**, eaaw0442 (2019). doi:10.1126/science.aaw0422/
4. E. Tatsumi et al., Spectrally blue hydrated parent body of asteroid (162173) Ryugu. *Nature Communications* **12**, 1–13 (2021). doi:10.1038/s41467-021-26071-8
5. E. Tatsumi et al., Collisional history of Ryugu's parent body from bright surface boulders. *Nature Astronomy* **5**, 39–45 (2021). doi:10.1038/s41550-020-1179-z
6. S. Tachibana et al., Pebbles and sand on asteroid (162173) Ryugu: In situ observation and particles returned to Earth. *Science* **375**, 1011-1016 (2021). doi:10.1126/science.abj8624
7. Materials and methods are available as supplementary materials.
8. F. Vilas, M. J. Gaffey, Phyllosilicate absorption features in main-belt and outer-belt asteroid reflectance spectra, *Science* **246**, 790-792 (1989). doi:10.1126/science.246.4931.790
9. P. Beck et al., Hydrous mineralogy of CM and CI chondrites from infrared spectroscopy and their relationship with low albedo asteroids. *Geochimica et Cosmochimica Acta* **74**, 4881–4892 (2010). doi:10.1016/j.gca.2010.05.020
10. D. Takir et al., Nature and degree of aqueous alteration in CM and CI carbonaceous chondrites. *Meteoritics & Planetary Science* **48**, 1618–1637 (2013). doi: 10.1111/maps.12171
11. O. Poch et al., Ammonium salts are a reservoir of nitrogen on a cometary nucleus and possibly on some asteroids. *Science* **367**, 332–340 (2020). doi:10.1126/science.aaw7462
12. T. Morota et all., Sample collection from asteroid (162173) Ryugu by Hayabusa2: Implications for surface evolution. *Science* **368**, 654–659 (2020). doi:10.1126/science.aaz6306
13. C. Pilorget et al., First compositional analysis of Ryugu samples by the MicrOmega hyperspectral microscope. *Nature Astronomy* **6**, 221–225 (2021), doi:10.1038/s41550-021-01549-z.

14. A. A. Simon et al., Widespread carbon-bearing materials on near-Earth asteroid (101955) Bennu. *Science* **370**, eabc3522 (2020). doi: 10.1126/science.abc3522
15. V. E. Hamilton et al., Evidence for limited compositional and particle size variation on asteroid (101955) Bennu from thermal infrared spectroscopy. *Astronomy & Astrophysics* **650**, A120 (2021). doi:10.1051/0004-6361/202039728
16. A. Bischoff et al., The old, unique C1 chondrite Flensburg–insight into the first processes of aqueous alteration, brecciation, and the diversity of water-bearing parent bodies and lithologies. *Geochimica et Cosmochimica Acta* ***293***, 142-186 (2021). doi: 10.2138/am-2017-6056
17. T. Yada et al., Preliminary analysis of the Hayabusa2 samples returned from C-type asteroid Ryugu. *Nature astronomy*, ISSN 2397-3366 (2021). doi:10.21203/RS.3.RS-608561/V1.
18. D. T. Britt, D. Yeomans, K. Housen, G. Consolmagno, "Asteroid density, porosity and structure" in *Asteroids III*, W. F. Bottke, A. Cellino, P. Paolicchi, R. P. Binzel, Eds. (University of Arizona Press, Tucson, 2002; http://www.jstor.org/stable/10.2307/j.ctv1v7zdn4), pp. 485–500.
19. C. P. Opeil, D. T. Britt, R. J. Macke, G. J. Consolmagno, The surprising thermal properties of CM carbonaceous chondrites. *Meteoritics & Planetary Science* **55**, E1-E20 (2020). doi:10.1111/maps.13556.
20. T. Okada et al., Highly porous nature of a primitive asteroid revealed by thermal imaging. *Nature* **579**, 518–522 (2020). doi:10.1038/s41586-020-2102-6
21. M. Hamm, I. Pelivan, M. Grott, and T. de Wiljes, Thermophysical parameter estimation of small Solar system bodies via data assimilation. *Monthly Notices Royal Astronomical Society* **496**, 2776-2785 (2020). doi:10.1093/mnras/staa1755
22. Y. Shimaki et al., Thermophysical properties of the surface of asteroid 162173 Ryugu: Infrared observations and thermal inertia mapping. *Icarus* **348** (2020), doi:10.1016/j.icarus.2020.113835.
23. D. J. Dunlop, Magnetism in rocks. Journal of Geophysical Research: *Solid Earth* **100**, 2161–2174 (1995). doi:10.1029/94JB02624
24. Ö. Özdemir, D. J. Dunlop, Effect of crystal defects and internal stress on the domain structure and magnetic properties of magnetite. Journal of Geophysical Research: *Solid Earth* **102**, 20211–20224 (1997). doi:10.1029/97JB01779
25. K. Shimomura et al., Superconducting muon channel at J-PARC. *Nuclear Instruments and Methods in Physics Research Section A: Accelerators, Spectrometers, Detectors and Associated Equipment* **600**, 192–194 (2009). doi:10.1016/j.nima.2008.11.029
26. K. Terada et al., A new X-ray fluorescence spectroscopy for extraterrestrial materials using a muon beam. *Scientific Reports* **4**, 5072 (2014). doi:10.1038/srep05072
27. K. Lodders, Relative atomic solar system abundances, mass fractions, and atomic masses of the elements and their isotopes, composition of the solar photosphere, and compositions of the major chondritic meteorite groups. *Space Science Reviews* **217**, 44 (2021). doi:10.1007/s11214-021-00825-8
28. M. Asplund, A. M. Amarsi, N. Grevesse, The chemical make-up of the Sun: A 2020 vision. *Astronomy & Astrophysics* **653**, A141 (2021). doi:10.1051/0004-6361/202140445

29. T. Yokoyama et al., The first returned samples from a C-type asteroid show kinship to the chemically most primitive meteorites. *Science* (2022), doi:10.1126/science.abn7850 .

30. E. Dartois et al., Dome C ultracarbonaceous Antarctic micrometeorites. *Astronomy & Astrophysics* **609**, A65 (2018). doi:10.1051/0004-6361/201731322

31. J. Alfing, M. Patzek, A. Bischoff, Modal abundances of coarse-grained (~5 μm) components within CI-chondrites and their individual clasts – Mixing of various lithologies on the CI parent body(ies). *Geochemistr*y **79**, 125532 (2019). doi:10.1016/j.chemer.2019.08.004

32. A. Morlok et al., Brecciation and chemical heterogeneities of CI chondrites. *Geochimica et Cosmochimica Acta* **70**, 5371–5394 (2006). doi:10.1016/j.gca.2006.08.007

33. A. J. King, P. F. Schofield, K. T. Howard, S. S. Russell, Modal mineralogy of CI and CI-like chondrites by X-ray diffraction. *Geochimica et Cosmochimica Acta* **165**, 148–160 (2015). doi:10.1016/j.gca.2015.05.038

34. K. Tomeoka, P. R. Buseck, Matrix mineralogy of the Orgueil CI carbonaceous chondrite. *Geochimica et Cosmochimica Acta* **52**, 1627–1640 (1988). doi:10.1016/0016-7037(88)90231-1

35. R. G. Burns, and D. S. Fisher, Rates of oxidative weathering on the surface of Mars. *J. Geophys. Res.*, **98(E2)**, 3365– 3372 (1993). doi:10.1029/92JE02055.

36. J. Booth, Q. Hong, R.G. Compton, K. Prout, R.M. Payne, Gypsum overgrowths passivate calcite to acid attack, *J. Colloid Interface Sci.*, **192**, 207-214 (1997). doi:10.1006/jcis.1997.4978

37. M. Gounelle, M. E. Zolensky, A terrestrial origin for sulfate veins in CI1 chondrites. *Meteoritics & Planetary Science* **36**, 1321–1329 (2001). doi:10.1111/j.1945-5100.2001.tb01827.x

38. M. Piralla, R. Tartèse, Y. Marrocchi, K. H. Joy, Apatite halogen and hydrogen isotope constraints on the conditions of hydrothermal alteration in carbonaceous chondrites. *Meteoritics & Planetary Science* **56**, 809–828 (2021). doi:10.1111/maps.13639

39. E. de Pauw et al., High energy synchrotron X-ray fluorescence trace element study of a millimeter-sized asteroidal particle in preparation for the Hayabusa2 return sample analyses. *Spectrochimica Acta Part B: Atomic Spectroscopy* **188**, 106346 (2022). doi:10.1016/j.sab.2021.106346

40. D. Ward, A. Bischoff, J. Roszjar, J. Berndt, M. J. Whitehouse, Trace element inventory of meteoritic Ca-phosphates. *American Mineralogist* **102**, 1856-1880 (2017). doi:10.2138/am-2017-6056

41. M. Endreß, “Mineralogische und chemische Untersuchungen an CI Chondriten – Ein Modell zur mineralogisch-kosmochemischen Evolution der(s) CI-Mutterkörper(s)” PhD thesis, University of Muenster (1994).

42. P. A. Bland, G. Cressey, O. N. Menzies, Modal mineralogy of carbonaceous chondrites by X-ray diffraction and Mössbauer spectroscopy. *Meteoritics & Planetary Science* **39**, 3–16 (2004). doi:10.1111/j.1945-5100.2004.tb00046.x

43. M. N. Bass, Montmorillonite and serpentine in Orgueil meteorite. *Geochimica et Cosmochimica Acta* **35**, 139–147 (1971). doi:10.1016/0016-7037(71)90053-6

44. S. M. Chemtob, R. D. Nickerson, R. v. Morris, D. G. Agresti, J. G. Catalano, Oxidative Alteration of Ferrous Smectites and Implications for the Redox Evolution of Early Mars. *Journal of Geophysical Research: Planets* **122**, 2469–2488 (2017). doi:10.1002/2017JE005331

45. S. Boursiquot, M. Mullet, M. Abdelmoula, J.-M. Génin, J.-J. Ehrhardt, The dry oxidation of tetragonal FeS_{1-x} mackinawite. *Physics and Chemistry of Minerals* **28**, 600–611 (2001). doi:10.1007/s002690100193

46. J. F. Kerridge, Major element composition of phyllosilicates in the Orgueil carbonaceous meteorite. *Earth and Planetary Science Letters* **29**, 194–200 (1976). doi:10.1016/0012-821X(76)90039-X

47. M. E. Zolensky, R. Barrett, L. Browning, Mineralogy and composition of matrix and chondrule rims in carbonaceous chondrites. *Geochimica et Cosmochimica Acta* 57, 3123–3148 (1993). doi:10.1016/0016-7037(93)90298-B

48. M. Endreß, A. Bischoff, Carbonates in CI chondrites: Clues to parent body evolution. *Geochimica et Cosmochimica Acta* 60, 489–507 (1996). doi:10.1016/0016-7037(95)00399-1

49. A. M. Reid, M. N. Bass, H. Fujita, J. F. Kerridge, K. Fredriksson, Olivine and pyroxene in the Orgueil meteorite. *Geochimica et Cosmochimica Acta* **34**, 1253–1255 (1970). doi:10.1016/0016-7037(70)90063-3

50. I. M. Steele, Minor elements in forsterites of Orgueil (C1), Alais (C1) and two interplanetary dust particles compared to C2-C3-UOC forsterites. *Meteoritics* **25**, 301–307 (1990). doi:10.1111/j.1945-5100.1990.tb00714.x

51. D. R. Frank, M. E. Zolensky, L. Le, Olivine in terminal particles of Stardust aerogel tracks and analogous grains in chondrite matrix. *Geochimica et Cosmochimica Acta* **142**, 240–259 (2014). doi:10.1016/j.gca.2014.05.037

52. M. R. Lee, K. Nicholson, Ca-carbonate in the Orgueil (CI) carbonaceous chondrite: Mineralogy, microstructure and implications for parent body history. *Earth and Planetary Science Letters*. **280**, 268–275 (2009). doi:10.1016/j.epsl.2009.01.038

53. I. D. R. Mackinnon, M. E. Zolensky, Proposed structures for poorly characterized phases in C2M carbonaceous chondrite meteorites. *Nature* **309**, 240–242 (1984). doi:10.1038/309240a0

54. J. P. Bradley, Chemically anomalous, preaccretionally irradiated Grains in Interplanetary dust from comets. *Science* **265**, 925–929 (1994). doi:10.1126/science.265.5174.925

55. H. Leroux, P. Cuvillier, B. Zanda, R. H. Hewins, GEMS-like material in the matrix of the Paris meteorite and the early stages of alteration of CM chondrites. *Geochimica et Cosmochimica Acta* **170**, 247–265 (2015). doi:10.1016/j.gca.2015.09.019

56. K. K. Ohtaki et al., Search for meteoritic GEMS I: Comparison of amorphous silicates in Paris and Acfer 094 chondrite matrices and in anhydrous chondritic interplanetary dust particles. *Geochimica et Cosmochimica Acta* **310**, 320–345 (2021). doi:10.1016/j.gca.2021.05.042

57. K. L. Villalon et al., Search for meteoritic GEMS II: Comparison of inclusions in amorphous silicates from the Paris chondrite and from anhydrous chondritic interplanetary dust particles. *Geochimica et Cosmochimica Acta* **310**, 346–362 (2021). doi:10.1016/j.gca.2021.05.041

58. T. Nakamura et al., Chondrulelike Objects in Short-Period Comet 81P/Wild 2. *Science* **321**, 1664–1667 (2008). doi:10.1126/science.1160995

59. D. R. Frank et al., A CAI in the Ivuna CI1 chondrite, *proceedings of the 42nd Lunar and Planetary Science Conference*, Abstract #2785, JSC-CN-22691 (2011)

60. T. J. Fagan, Y. Guan, G. J. MacPherson, Al-Mg isotopic evidence for episodic alteration of Ca-Al-rich inclusions from Allende. *Meteoritics & Planetary Science* **42**, 1221–1240 (2007). doi:10.1111/j.1945-5100.2007.tb00570.x

61. W. Klöck, K. L. Thomas, D. S. McKay, H. Palme, Unusual olivine and pyroxene composition in interplanetary dust and unequilibrated ordinary chondrites. *Nature* **339**, 126–128 (1989). doi:10.1038/339126a0

62. L. Grossman, I. M. Steele, Amoeboid olivine aggregates in the Allende meteorite. *Geochimica et Cosmochimica Acta* **40**, 149–155 (1976). doi:10.1016/0016-7037(76)90172-1

63. J. Han, A. J. Brearley, Microstructural evidence for complex formation histories of amoeboid olivine aggregates from the ALHA77307 CO3.0 chondrite. *Meteoritics & Planetary Science*. **50**, 904–925 (2015). doi: 10.1111/maps.12439

64. A. Tsuchiyama, A. Miyake, S. Okuzumi, A. Kitayama, J. Kawano, K. Uesugi, A. Takeuchi, T. Nakano, M. E. Zolensky, Discovery of primitive CO_2-bearing fluid in an aqueously altered carbonaceous chondrite. *Science Advances* **7**, 9707–9728 (2021). doi: 10.1126/sciadv.abg9707

65. M. E. Zolensky, Cyclical regolith processes on hydrous asteroids. *Meteoritics* **30**, abstract 606-607 (1995). (available at https://ui.adsabs.harvard.edu/abs/1995Metic..30Q.606Z/abstract)

66. L. Zhang, F. Ren, H. Li, D. Cheng, B. Sun, The influence mechanism of freeze-thaw on soil erosion: A review. *Water* **13**, 1010 (2021). doi:10.3390/w13081010

67. D. J. Vaughan, *Mineral chemistry of metal sulfides* (Cambridge Earth Sci. Ser., Cambridge, 493. 1978). doi:10.1016/0012-8252(80)90122-1

68. T. Nakamura et al., Irradiation-energy dependence on the spectral changes of hydrous C-type asteroids based on 4keV and 20keV He exposure experiments of Murchison CM chondrite, *proceedings of the 51st Lunar and Planetary Science Conference*, Abstract #1310 (2020).

69. K. Tomeoka, Y. Yamahana, T. Sekine, Experimental shock metamorphism of the Murchison CM carbonaceous chondrite. *Geochimica et Cosmochimica Acta* **63**, 3683–3703 (1999). doi:10.1016/S0016-7037(99)00149-0

70. D. Beaufort et al., Chlorite and chloritization processes through mixed-layer mineral series in low-temperature geological systems – a review. *Clay Minerals* **50**, 497–523 (2015). doi:10.1180/claymin.2015.050.4.06

71. S. A. Kissin, S. D. Scott, Phase relations involving pyrrhotite below 350 degrees C. *Economic Geology* **77**, 1739–1754 (1982). doi:10.2113/gsecongeo.77.7.1739

72. E. L. Berger, D. S. Lauretta, T. J. Zega, L. P. Keller, Heterogeneous histories of Ni-bearing pyrrhotite and pentlandite grains in the CI chondrites Orgueil and Alais. *Meteoritics & Planetary Science* **51**, 1813–1829 (2016). doi:10.1111/maps.12721

73. R. Visser, T. John, M. Patzek, A. Bischoff, M. J. Whitehouse, Sulfur isotope study of sulfides in CI, CM, $C2_{ung}$ chondrites and volatile-rich clasts – Evidence for different generations and reservoirs of sulfide formation. *Geochimica et Cosmochimica Acta* **261**, 210223 (2019). doi:10.1016/j.gca.2019.06.046

74. K. Tsukimura, H. Nakazawa, T. Endo, O. Fukunaga, Cation distribution in pentlandites $(Fe,Ni)_9S_8$: Dependence on pressure and temperature and kinetics of the cation exchange reaction. *Physics and Chemistry of Minerals* **19** (1992), doi:10.1007/BF00202309.

75. K. Sugiyama, T. Kawamata, T. Kuribayashi, Structure refinement of prehnite from Passaic County, New Jersey, USA, *Journal of Mineralogical and Petrological Sciences*, 210318 (2021) doi:10.2465/jmps.210318

76. H.-B. Qin, Y. Takeichi, H. Nitani, Y. Terada, Y. Takahashi, Tellurium Distribution and Speciation in Contaminated Soils from Abandoned Mine Tailings: Comparison with Selenium. *Environmental Science & Technology*. **51**, 6027–6035 (2017).

77. Y. Takeichi, N. Inami, H. Suga, C. Miyamoto, T. Ueno, K. Mase, Y. Takahashi, K. Ono, Design and performance of a compact scanning transmission X-ray microscope at the Photon Factory. *Review of Scientific Instruments* **87**, 013704 (2016). doi:10.1063/1.4940409

78. C. A. Gorski, L. E. Klüpfel, A. Voegelin, M. Sander, T. B. Hofstetter, Redox properties of structural Fe in clay minerals: 3. Relationships between smectite redox and structural properties. *Environmental Science & Technology* **47**, 13477–13485 (2013). doi:10.1021/es403824x

79. P. Lu, C. Zhu, Arsenic Eh-pH diagrams at 25°C and 1 bar. *Environmental Earth Sciences* **62**, 1673–1683 (2011). doi:10.1007/s12665-010-0652-x

80. K. Fukushi, Y. Sekine, H. Sakuma, K. Morida, R. Wordsworth, Semiarid climate and hyposaline lake on early Mars inferred from reconstructed water chemistry at Gale. *Nature communications* **10**, 1-11 (2019). doi:10.1038/s41467-019-12871-6

81. C. M. O'D. Alexander, R. Bowden, M. L. Fogel, K. T. Howard, Carbonate abundances and isotopic compositions in chondrites. *Meteoritics & Planetary Science* **50**, 810–833 (2015).

82. M. Yu. Zolotov, Aqueous fluid composition in CI chondritic materials: Chemical equilibrium assessments in closed systems. *Icarus* **220**, 713–729 (2012). doi:10.1016/j.icarus.2012.05.036

83. M. Yu. Zolotov, Formation of sulfates on parent bodies of carbonaceous chondrites, Ceres, Europa, and other icy bodies, *proceedings of the 47th Lunar and Planetary Science Conference*, Abstract #1903 (2016)

84. H. Campins et al., The origin of asteroid 162173 (1999 JU3). *The Astronomical Journal*. **146**, 26 (2013). doi:10.1088/0004-6256/146/2/26

85. K. J. Walsh, M. Delbó, W. F. Bottke, D. Vokrouhlický, D. S. Lauretta, Introducing the Eulalia and new Polana asteroid families: Re-assessing primitive asteroid families in the inner Main Belt. *Icarus* **225**, 283–297 (2013). doi:10.1016/j.icarus.2013.03.005

86. H. Wang et al., Lifetime of the solar nebula constrained by meteorite paleomagnetism. *Science* **355**, 623–627 (2017). doi:10.1126/science.aaf5043

87. K. L. Thomas, G. E. Blanford, L. P. Keller, W. Klöck, D. S. McKay, Carbon abundance and silicate mineralogy of anhydrous interplanetary dust particles. *Geochimica et Cosmochimica Acta*. **57**, 1551–1566 (1993). doi:10.1016/0016-7037(93)90012-L

88. M. J. Mumma, S. B. Charnley, The Chemical Composition of Comets—Emerging Taxonomies and Natal Heritage. *Annual Review of Astronomy and Astrophysics* **49**, 471–524 (2011). doi:10.1146/annurev-astro-081309-130811

89. S. J. Desch, A. Kalyaan, C. M. O'D. Alexander, The Effect of Jupiter's Formation on the Distribution of Refractory Elements and Inclusions in Meteorites. *The Astrophysical Journal Supplement Series* **238**, 11 (2018). doi:10.3847/1538-4365/aad95f

90. P. Michel et al., Collisional formation of top-shaped asteroids and implications for the origins of Ryugu and Bennu. *Nature Communications* **11**, 2655 (2020). doi:10.1038/s41467-020-16433-z

91. A. A. Amsden, H. M. Ruppel, C. W. Hirt, SALE: a simplified ALE computer program for fluid flow at all speeds, *OSTI. GOV/Technical Report* (1980), doi:10.2172/5176006

92. B. A. Ivanov, D. Deniem, G. Neukum, Implementation of dynamic strength models into 2D hydrocodes: Applications for atmospheric breakup and impact cratering. *International Journal of Impact Engineering* **20**, 411–430 (1997). doi:10.1016/S0734-743X(97)87511-2

93. K. Wünnemann, G. S. Collins, H. J. Melosh, A strain-based porosity model for use in hydrocode simulations of impacts and implications for transient crater growth in porous targets. *Icarus* **180**, 514–527 (2006). doi:10.1016/j.icarus.2005.10.013

94. W. F. Bottke, M. C. Nolan, R. Greenberg, R. A. Kolvoord, Velocity distributions among colliding asteroids. *Icarus* **107**, 255–268 (1994). doi:10.1006/icar.1994.1021

95. V. E. Hamilton et al., Evidence for widespread hydrated minerals on asteroid (101955) Bennu. *Nature Astronomy* **3**, 332–340 (2019). doi:10.1038/s41550-019-0722-2

96. P. Beck et al., Transmission infrared spectra (2-25μm) of carbonaceous chondrites (CI, CM, CV-CK, CR, C2 ungrouped): Mineralogy, water, and asteroidal processes. *Icarus*. **229**, 263–277 (2014). doi:10.1016/j.icarus.2013.10.019

97. Koprinarov, I. N., Hitchcock, A. P., McCrory, C. T., and Childs, R. F. (2002). Quantitative mapping of structured polymeric systems using singular value decomposition analysis of soft X-ray images. *The Journal of Physical Chemistry B*, **106(21)**, 5358-5364. **DOI**

98. M. Toplak et al., Infrared Orange: Connecting hyperspectral data with machine learning. *Synchrotron Radiation News* **30**, 40–45 (2017). doi:10.1080/08940886.2017.1338424

99. R. Brunetto et al., Characterizing irradiated surfaces using IR spectroscopy. *Icarus* **345**, 113722 (2020). doi:10.1016/j.icarus.2020.113722

100. R. H. Hewins et al., NORTHWEST AFRICA (NWA) 12563 and ungrouped C2 chondrites: Alteration styles and relationships to asteroids. *Geochimica et Cosmochimica Acta* **311**, 238–273 (2021). doi:10.1016/j.gca.2021.06.035

101. M. Arakawa et al., An artificial impact on the asteroid (162173) Ryugu formed a crater in the gravity-dominated regime. *Science* **368**, 18 (2020). doi:10.1126/science.aaz1701

102. M. Uesugi, K. Uesugi, M. Oka, Non-destructive observation of meteorite chips using quantitative analysis of optimized X-ray micro-computed tomography. *Earth and Planetary Science Letters* **299**, 359–367 (2010). doi:10.1016/j.epsl.2010.09.016

103. M. Uesugi et al., Three-dimensional observation of carbonaceous chondrites by synchrotron radiation X-ray CT – Quantitative analysis and develo pments for the future sample return missions. *Geochimica et Cosmochimica Acta* **116**, 17–32 (2013). doi:10.1016/j.gca.2012.09.025

104. M. Uesugi et al, Development of a sample holder for synchrotron radiation-based computed tomography and diffraction analysis of extraterrestrial materials. *Review of Scientific Instruments* **91**, 035107 (2020). doi:10.1063/1.5122672

105. T. Nakamura et al., Itokawa Dust Particles: A Direct Link Between S-Type Asteroids and Ordinary Chondrites. *Science* **333**, 1113–1116 (2011). doi:10.1126/science.1207758

106. D. Nakashima et al., Ion microprobe analyses of oxygen three-isotope ratios of chondrules from the Sayh al Uhaymir 290 CH chondrite using a multiple-hole disk. *Meteoritics & Planetary Science* **46**, 857–874 (2011). doi:10.1111/J.1945-5100.2011.01198.X

107. C. E. Moyano-Cambero et al., Nanoindenting the Chelyabinsk meteorite to learn about impact deflection effects in asteroids. *The Astrophysical Journal* **835**, 157 (2017). doi:10.3847/1538-4357/835/2/157

108. S. Tanbakouei et al., Mechanical properties of particles from the surface of asteroid 25143 Itokawa. *Astronomy & Astrophysics* **629**, A119 (2019). doi:10.1051/0004-6361/201935380

109. J. D. James, J. A. Spittle, S. G. R. Brown, R. W. Evans, A review of measurement techniques for the thermal expansion coefficient of metals and alloys at elevated temperatures. *Measurement Science and Technology* **12**, R1 (2001). doi:10.1088/0957-0233/12/3/201

110. Y. Nagaashi, T. Aoki, A. M. Nakamura, Cohesion of regolith: Measurements of meteorite powders. *Icarus*. **360**, 114357 (2021). doi:10.1016/j.icarus.2021.114357

111. H. K. D. H. Bhadeshia, Differential Scanning Calorimetry, University of Cambridge, Materials Science & Metallurgy, (available at www.phase-trans.msm.cam.ac.uk/2002/Thermal2.pdf).

112. H. S. Carslaw, J. C. Jaeger, *Conduction of Heat in Solids*, (Oxford University Press, Oxford, 1986).

113. T. Ishizaki, H. Nagano, Measurement of 3D thermal diffusivity distribution with lock-in thermography and application for high thermal conductivity CFRPs. *Infrared Physics & Technology* **99**, 248–256 (2019). doi:10.1016/j.infrared.2019.04.023

114. T. Ishizaki, H. Nagano, Measurement of Three-dimensional anisotropic thermal diffusivities for carbon fiber-reinforced plastics using lock-in thermography. *International Journal of Thermophysics* **36**, 2577–2589 (2015). doi:10.1007/s10765-014-1755-5

115. A. Tatami, M. Tachibana, T. Yagi, M. Murakami, Preparation of multilayer graphene sheets and their applications for particle accelerators. *AIP Conference Proceedings*. **1962**, 030005 (2018). doi:10.1063/1.5035522

116. D. Souda et al., High Thermoelectric Power Factor of Si-Mg2Si Nanocomposite Ribbons Synthesized by Melt Spinning. *ACS Applied Energy Materials*. **3**, 1962–1968 (2020). doi:10.1021/acsaem.9b02395

117. R. Abe et al., Round robin study on thermal conductivity/diffusivity of a gold wire with diameter of 30 mm tested by five measurement methods, *Journal of Thermal Science*, **31**, 1037–1051 (2022). https://doi.org/10.1007/s11630-022-1594-9

118. R. J. Knight, A. Nur, The dielectric constant of sandstones, 60 kHz to 4 MHz. *Geophysics* **52**, 644–654 (1987). doi:10.1190/1.1442332

119. J. Gattacceca, P. Rochette, Toward a robust normalized magnetic paleointensity method applied to meteorites. *Earth and Planetary Science Letters* **227**, 377–393 (2004). doi:10.1016/j.epsl.2004.09.013

120. D. J. Dunlop, O. Ozdemir, *Rock Magnetism. Fundamentals and Frontiers* (Cambridge University Press, Cambridge, 1997).

121. Y. Kimura et al., Vortex magnetic structure in framboidal magnetite reveals existence of water droplets in an ancient asteroid. *Nature Communications* **4**, 1–8 (2013). doi:10.1038/ncomms3649

122. J. T. Armstrong, CITZAF-a package of correction programs for the quantitative electron microbeam X-Ray-analysis of thick polished materials, thin-films, and particles. *Microbeam Analysis* **4**, 177–200 (1995).

123. A. Tsuchiyama et al. , Analytical dual-energy microtomography: A new method for obtaining three-dimensional mineral phase images and its application to Hayabusa samples. *Geochimica et Cosmochimica Acta* **116**, 5–16 (2013). doi:10.1016/j.gca.2012.11.036

124. A. Takeuchi, K. Uesugi, Y. Suzuki, Three-dimensional phase-contrast X-ray microtomography with scanning–imaging X-ray microscope optics. *Journal of Synchrotron Radiation* **20**, 793–800 (2013). doi:10.1107/S0909049513018876

125. M. Matsumoto et al., Discovery of fossil asteroidal ice in primitive meteorite Acfer 094. *Science Advances* **5**, 793–800 (2019). doi:10.1126/sciadv.aax5078

126. W. Sturhahn, CONUSS and PHOENIX: Evaluation of nuclear resonant scattering data. *Hyperfine Interactions* **125**, 149–172 (2000). doi:10.1023/A:1012681503686

127. L. Zhang et al., Optimizing X-ray mirror thermal performance using matched profile cooling. *Journal of Synchrotron Radiation* **22**, 1170–1181 (2015). doi:10.1107/S1600577515013090

128. E. de Grave, A. van Alboom, Evaluation of ferrous and ferric Mössbauer fractions. *Physics and Chemistry of Minerals* **18**, 337–342 (1991). doi: 10.1007/BF00200191

129. M. D. Dyar, M. W. Schaefer, E. C. Sklute, J. L. Bishop, Mössbauer spectroscopy of phyllosilicates: effects of fitting models on recoil-free fractions and redox ratios. *Clay Minerals* **43** (2008), 3-33. doi:10.1180/claymin.2008.043.1.02

130. M. Roskosz et al., Structural, redox and isotopic behaviors of iron in geological silicate glasses: A NRIXS study of Lamb-Mössbauer factors and force constants. *Geochimica et Cosmochimica Acta* **321**, 184-205 (2022) doi: 10.1016/j.gca.2022.01.021

131. C. Prescher, V. B. Prakapenka, DIOPTAS : a program for reduction of two-dimensional X-ray diffraction data and data exploration. *High Pressure Research* **35**, 223–230 (2015). doi:10.1080/08957959.2015.1059835

132. B. H. Toby, R. B. von Dreele, GSAS-II : the genesis of a modern open-source all purpose crystallography software package. *Journal of Applied Crystallography* **46**, 544–549 (2013). doi:10.1107/S0021889813003531

133. M. B. Madsen, S. Morup, T. V. V. Costa, J. M. Knudsen, M. Olsen, Superparamagnetic component in the Orgueil meteorite and Mössbauer spectroscopy studies in applied magnetic fields. *Nature* **321,** 501-503 (1986). doi:10.1038/321501a0

134. D. Gournis, A. E. Mantaka-Marketou, M. A. Karakassides, D. Petridis, Effect of γ-irradiation on clays and organoclays: a Mössbauer and XRD study. *Physics and Chemistry of Minerals* **27**, 514–521 (2000). doi:10.1007/s002690000089

135. L. M. Rodríguez-Lorenzo, J. N. Hart, K. A. Gross, Influence of fluorine in the synthesis of apatites. Synthesis of solid solutions of hydroxy-fluorapatite, *Biomaterials* **24**, 3777-3785 (2003). doi:10.1016/S0142-9612(03)00259-X

136. Y. Yokoyama, K. Tanaka, Y. Takahashi, Differences in the immobilization of arsenite and arsenate by calcite, *Geochimica et Cosmochimica Acta* **91**, 202-219 (2012). doi:10.1016/j.gca.2012.05.022

137. G. Schmid et al., Synchrotron-based chemical nano-tomography of microbial cell-mineral aggregates in their natural, hydrated state. *Microscopy and Microanalysis* **20**, 531-536 (2014). doi:10.1017/S1431927613014104

138. P. A. van Aken, B. Liebscher, Quantification of ferrous/ferric ratios in minerals: new evaluation schemes of Fe L_{23} electron energy-loss near-edge spectra. *Physics and Chemistry of Minerals* **29**, 188-200 (2002). doi:10.1007/s00269-001-0222-6

139. V. A. Solé, E. Papillon, M. Cotte, P. Walter, J. Susini, A multiplatform code for the analysis of energy-dispersive X-ray fluorescence spectra. *Spectrochimica Acta Part B: Atomic Spectroscopy* **62**, 63–68 (2007). doi:10.1016/J.SAB.2006.12.002

140. D. Gürsoy, F. de Carlo, X. Xiao, C. Jacobsen, TomoPy: a framework for the analysis of synchrotron tomographic data. *Journal of Synchrotron Radiation* **21**, 1188–1193 (2014). doi:10.1107/S1600577514013939

141. B. A. Dowd, G. H. Campbell, R. B. Marr, V. v. Nagarkar, S. v. Tipnis, L. Axe, D. P. Siddons, Developments in synchrotron X-ray computed microtomography at the National Synchrotron Light Source. *Developments in X-Ray Tomography II* **3772**, 224–236 (1999). doi:10.1117/12.363725

142. M. E. Zolensky, W. L. Bourcier, J. L. Gooding, Aqueous alteration on the hydrous asteroids: Results of EQ3/6 computer simulations. *Icarus* **78**, 411–425 (1989). doi:10.1016/0019-1035(89)90188-7

143. C. M. O'D. Alexander et al., The nature, origin and modification of insoluble organic matter in chondrites, the major source of Earth's C and N, *Geochemistry* **77**, 227-256 (2017) doi:10.1016/j.chemer.2017.01.007

144. M. Yu. Zolotov, M. V. Mironenko, Hydrogen chloride as a source of acid fluids in parent bodies of chondrites. *proceedings of the 38th Lunar and Planetary Science Conference*, Abstract #2340 (2007). https://www.lpi.usra.edu/meetings/lpsc2007/pdf/2340.pdf

145. J. S. Seewald, M. Yu. Zolotov, T. McCollom, Experimental investigation of single carbon compounds under hydrothermal conditions. *Geochimica et Cosmochimica Acta* **70**, 446–460 (2006). doi:10.1016/j.gca.2005.09.002

146. M. Yu. Zolotov, M. V. Mironenko, E. L. Shock, Thermodynamic constraints on fayalite formation on parent bodies of chondrites. *Meteoritics & Planetary Science* **41**, 1775–1796 (2006). doi:10.1111/J.1945-5100.2006.TB00451.X

147. S. Okuzumi, M. Momose, S. Sirono, H. Kobayashi, H. Tanaka, Sintering-induced dust ring formation in protoplanetary disks: Application to the HL tau disk. *The Astrophysical Journal* **821**, 82 (2016). doi:10.3847/0004-637X/821/2/82

148. J. N. Connelly et al., The absolute chronology and thermal processing of solids in the solar protoplanetary disk. *Science* **338**, 651–655 (2012). doi:10.1126/science.1226919

149. K. Lodders, Solar System Abundances and Condensation Temperatures of the Elements. *The Astrophysical Journal* **591**, 1220–1247 (2003). doi:10.1086/375492

150. D. N. Schramm, F. Tera, G. J. Wasserburg, The isotopic abundance of 26Mg and limits on26Al in the early solar system. *Earth and Planetary Science Letters* **10**, 44–59 (1970). doi:10.1016/0012-821X(70)90063-4

151. W. M., Haynes, *CRC handbook of chemistry and physics*, (CRC Press, Boca Raton, Florida, Ed. 91, 2010).

152. S. Wakita, M. Sekiya, Thermal evolution of icy planetesimals in the solar nebula. *Earth, Planets and Space*. **63**, 1193–1206 (2011). doi:10.5047/eps.2011.08.012

153. L. M. Shulman, The heat capacity of water ice in interstellar or interplanetary conditions. *Astronomy & Astrophysics* **416**, 187-190 (2016).

154. D. M. Murphy, T. Koop, Review of the vapour pressures of ice and supercooled water for atmospheric applications. *Quarterly Journal of the Royal Meteorological Society* **131**, 1539–1565 (2005). doi:10.1256/QJ.04.94

155. J. H. Tillotson, Metallic equations of state for hypervelocity impact, General Atomic Reports, GA-3216 (1962). (available at https://apps.dtic.mil/sti/citations/AD0486711).

156. W. Benz, E. Asphaug, Catastrophic Disruptions Revisited. *Icarus* **142**, 5–20 (1999). doi:10.1006/ICAR.1999.6204

157. B. A. Ivanov, F. Langenhorst, A. Deutsch, U. Hornemann, How strong was impact-induced CO_2 degassing in the Cretaceous-Tertiary event? Numerical modeling of shock recovery experiments. *Special Paper of the Geological Society of America* **356**, 587–594 (2002). doi:10.1130/0-8137-2356-6.587

158. K. Kurosawa, T. Okamoto, H. Genda, Hydrocode modeling of the spallation process during hypervelocity impacts: Implications for the ejection of Martian meteorites. *Icarus* **301**, 219–234 (2018). doi:10.1016/j.icarus.2017.09.015

159. R. Hyodo, K. Kurosawa, H. Genda, T. Usui, K. Fujita, Transport of impact ejecta from Mars to its moons as a means to reveal Martian history. *Scientific Reports*. **9**, 1–6 (2019). doi:10.1038/s41598-019-56139-x

160. T. Okamoto, K. Kurosawa, H. Genda, T. Matsui, Impact ejecta near the impact point observed using ultra-high-speed imaging and SPH simulations and a comparison of the two

methods. *Journal of Geophysical Research: Planets* **125**, e2019JE005943 (2020). doi:10.1029/2019JE005943

161. H. J. Melosh, Impact cratering: a geologic process. (Oxford University Press, 1989).

162. M. A. Meyers, *Dynamic Behavior of Materials* (Wiley, 1994). doi:10.1002/9780470172278

163. W. W. Anderson, T. J. Ahrens, Shock wave equations of state of chondritic meteorites. *AIP Conference Proceedings*. **429**, 115-118 (1998). doi:10.1063/1.55475

164. K. Kurosawa et al., Ryugu's observed volatile loss did not arise from impact heating alone. *Communications Earth & Environment* **2**, 1–6 (2021). doi:10.1038/s43247-021-00218-3

165. M. Lazzarin, C. Barbieri, M. A. Barucci, Visible spectroscopy of dark, primitive asteroids. The Astronomical Journal 110, 3058–3072 (1995). doi: 10.1086/117747

166. R. Hyodo, H. Genda, Implantation of Martian Materials in the Inner Solar System by a Mega Impact on Mars. *The Astrophysical Journal Letters* **856**, L36 (2018). doi:10.3847/2041-8213/aab7f0

167. G. S. Collins et al., *iSALE-Dellen manual*. Figshare (2016). doi:10.6084/m9.figshare.3473690.v2

168. E. Pierazzo et al., Validation of numerical codes for impact and explosion cratering: Impacts on strengthless and metal target. *Meteoritics & Planetary Science* **43**, 1917-1938 (2008). doi:10.1111/j.1945-5100.2008.tb00653.x

169. S. N. Quintana, D. A. Crawford, P. H. Schultz, Analysis of Impact Melt and Vapor Production in CTH for Planetary Applications. *Procedia Engineering* **103**, 499–506 (2015). doi:10.1016/J.PROENG.2015.04.065

170. K. Kurosawa, H. Genda, Effects of friction and plastic deformation in shock-comminuted damaged rocks on impact heating, *Geophysical Research Letters* **45**, 620-626 (2018). doi: 10.1002/2017GL076285

171. D. C. Drucker, W. Prager, Soil mechanics and plastic analysis or limit design. *Quarterly of applied mathematics* **10**, 157–165 (1952).

172. M. Ohnaka, A shear failure strength law of rock in the brittle-plastic transition regime. *Geophysical Research Letters* **22**, 25–28 (1995). doi:10.1029/94GL02791

173. D. Ostrowski, K. Bryson, The physical properties of meteorites. *Planetary and Space Science* **165**, 148–178 (2019). doi:10.1016/J.PSS.2018.11.003

174. J.-C. Viennet et al., Effect of particle size on the experimental dissolution and auto-aluminization processes of K-vermiculite. *Geochimica et Cosmochimica Acta* **180**, 164–176 (2016). doi:10.1016/j.gca.2016.02.005

175. E. Ferrage, Investigation of smectite hydration properties by modeling experimental X-ray diffraction patterns: Part I. Montmorillonite hydration properties. *American Mineralogist* **90**, 1358–1374 (2005). doi:10.2138/am.2005.1776

176. J. -C. Viennet et al., Investigation of clay mineralogy in a temperate acidic soil of a forest using X-ray diffraction profile modeling: Beyond the HIS and HIV description. *Geoderma* **241–242**, 75–86 (2015). doi:10.1016/j.geoderma.2014.11.004

~~177.H. Uesugi, M. Uesugi, T. Tani, Image processing scheme for archiving epigraphs, in *2018 3rd Digital Heritage International Congress (DigitalHERITAGE) held jointly with 2018 24th International Conference on Virtual Systems & Multimedia (VSMM 2018)*, pp. 1–8. doi: 10.1109/DigitalHeritage.2018.8810059~~

178.“Differential Scanning Calorimetry.” NETZSCH Análisis & Ensayo, https://www.netzsch-thermal-analysis.com/es/industrias-sectores/methods/differential-scanning-calorimetry/.

179.S. W. Kieffer, C. H. Simonds, The role of volatiles and lithology in the impact cratering process. *Reviews of Geophysics* **18** (1980), pp. 143–181. doi:10.1029/RG018i001p00143

180.T. Sekine, T. Kobayashi, M. Nishio, E. Takahashi, Shock equation of state of basalt. *Earth, Planets and Space* **60**, 999–1003 (2008). doi:10.1186/BF03352857

181.T. J. Ahrens, J. D. O’Keefe, Shock melting and vaporization of lunar rocks and minerals. *The Moon* **4**, 214–249 (1972). doi:10.1007/BF00562927

182.E. Pierazzo, D. A. Kring, H. Jay Melosh, Hydrocode simulation of the Chicxulub impact event and the production of climatically active gases. *Journal of Geophysical Research: Planets* **103**, 28607–28625 (1998). doi:10.1029/98JE02496

183.A. Tsuchiyama et al., Strength measurements of carbonaceous chondrites and cosmic dust analogs using micro compression testing machine, *Proceedings of Japan Geoscience Union Annual Meeting*, Abstract #168-002 (2008). (available at http://www2.jpgu.org/meeting/2008/program/pdf/P168/P168-002_e.pdf)

184.V. V. Svetsov, I. V. Nemtchinov, A. V. Teterev, Disintegration of Large Meteoroids in Earth’s Atmosphere: Theoretical Models. *Icarus* **116**, 131–153 (1995). doi:10.1006/icar.1995.1116

185.C. P. Opeil, G. J. Consolmagno, D. T. Britt, The thermal conductivity of meteorites: New measurements and analysis. *Icarus* **208**, 449–454 (2010). doi:10.1016/j.icarus.2010.01.021

186.G. J. Consolmagno et al., The measurement of meteorite heat capacity at low temperatures using liquid nitrogen vaporization. *Planetary and Space Science*. **87**, 146–156 (2013). doi:10.1016/j.pss.2013.07.009

187.R. J. Macke, G. J. Consolmagno, D. T. Britt, Density, porosity, and magnetic susceptibility of carbonaceous chondrites. *Meteoritics & Planetary Science*. **46**, 1842–1862 (2011). doi:10.1111/J.1945-5100.2011.01298.X

188.M. Szurgot, Thermal conductivity of meteorites, The 74th Annual Meteoritical Society Meeting, Abstract #5074 (2011).

189.A. Brecher, P. L. Briggs, G. Simmons, The low-temperature electrical properties of carbonaceous meteorites. *Earth and Planetary Science Letters* **28**, 37–45 (1975). doi:10.1016/0012-821X(75)90071-0

190.P. Rochette et al., Magnetic classification of stony meteorites: 2. Non-ordinary chondrites. *Meteoritics & Planetary Science* **43**, 959–980 (2008). doi:10.1111/j.1945-5100.2008.tb01092.x

191.S. Sridhar, J. F. J. Bryson, A. J. King, R. J. Harrison, Constraints on the ice composition of carbonaceous chondrites from their magnetic mineralogy, *Earth and Planetary Science Letters* **576**, 117243 (2021) doi:10.1016/j.epsl.2021.117243

192. E. Ibrahim, “The elastic properties of carbonaceous chondrites” Master’s thesis, University of Calgary, Calgary, AB (2012). doi:10.11575/PRISM/28122

193. T. M. Davison, G. S. Collins, P. A. Bland, Mesoscale modeling of impact compaction of primitive solar system solids, *The Astrophysical Journal* **821**, 68 (2016). doi:10.3847/0004-637X/821/1/68

Acknowledgments:
Synchrotron time for XRD and STXM analyses was allocated by the Photon Factory Advisory Committee (proposal numbers 2020S2-002 and 2018S1-001). The SR-CT and μ-XRF-XANES analyses were conducted under SPring-8 proposal numbers 2019A-2021A0165, 2019A-2021A0166, 2021B0185, and 2021B0188, and 2022A0180. Technical supports in the SR experiments at SPring-8 were providedby RIKEN. The negative muon analysis at MLF, J-PARC was conducted under proposal number 2019MS01.

Numerical computations for the thermal modelling were carried out on the PC cluster and analysis servers at the Center for Computational Astrophysics of the National Astronomical Observatory of Japan. We thank the developers of iSALE, including G. Collins, K. Wünnemann, B. Ivanov, J. Melosh, D. Elbeshausen, and T. Davison.

This research used resources of the Advanced Photon Source, a U.S. Department of Energy (DOE) Office of Science User Facility at Argonne National Laboratory

We thank A. Simon and V. Hamilton for providing the spectra of asteroid Bennu, and Toyo Corporation for the use of the pFIB system for sample preparation.

We also thank many researchers who have contributed to the various experiments and measurements, especially H. Nakao, R. Watanabe, S. Kobayashi, K. Mogi, Y. Kousaka, E. Tomosada, T. Morita, M. Nakamura, O. Sasaki, K. Saito, T. Konno, T. Miyazaki, Y. Ito, K. Onodera, S. Hasegawa, G. Nishikawa, T. Kobayashi, S. Murakoshi, K. Goto, Y. Tanaka, K. Hattori, M. Yoshioka, K. Tomioka, T. Kawahara, S. Tachikawa, T. Nishi, H. Ohta, M. Susa, T. Sunagawa, O. Nishizawa, K. Kitamura, K. Sawayama, T. Hatakeyama, S. Steve, S. Sutton, R. Jones, R. Yoshida, H. Kasai, T. Akashi, I. Hitachi, A. Dazzi, A. Deniset-Besseau, L. Bejach, J. Garrevoat, M. Michiel, T. Azuma, K. Mizumoto, T. Minami, K. Shimomura, S. Takeda, M. Katsuragawa, A. Yamaguchi, T. Yomogida, D. Wakabayashi, J. Garrevoet, M. di Michiel, O. Mivumbi, C. Sandt, Z. Rahman, L. Le, F. Capitani, and Shimazu Corporation for their technical support.

Funding: Supported by KAKENHI from the Japanese Society for Promotion of Science (JSPS), grants JP20H00188 and 19H05183 to T.N., JP19K14776 to M.M., JP20H00205 to A.Ts., M.M., A.M. and J.M., 17H06458 to K.F., Y.T., S.Y. and M.K., JP17H06459 to T.N., T.U., S.W., M.M., N.N., T.M., T.O., Y.S., N.S., and R.N., JP15H05695 to A.Ts. and K.U., 20H05846 to S.T., JP17H06457 to H.G., JP17H06458 to Y. T. and K. F., JP19H00726 to K.K., H. G., and T.M., JP21J13337 to K.A., and JP18H05456,JP20H00189 to K.S., 18H05463 to T.T., S.N., and S.W., 18H05460 to K.N. and T.O., 18H05464 to Y.M., 18H05457 to K.N., T.T., S.W., and Y.M., and JP18H05479 to M.U. Also supported by the JSPS Core-to-Core program “ International Network of Planetary Sciences”, and from the Ministry of Education, Culture, Sports, Science and Technology (MEXT) (grants JPMXS0450200421 and JPMXS0450200521) to SS.

A.K. acknowledges funding support from UK Research and Innovation (UKRI) grant MR/T020261/1.

A.B. acknowledges funding support from NASA Emerging Worlds grant - 80NSSC18K0731.

P.B. acknowledges funding from the European Research Council (ERC) under grant agreement no. 771691 (Solarys) and the Centre National d'Etude Spatiale (CNES).

B.T. acknowledges funding from German Research Foundation DFG grant BR2015/38-1 and Dr. Ralph Schwieter Foundation.

P. T. acknowledges funding from Ghent University Special Research Fund Grants BOF20/PDO/037 and Research Foundation Flanders grants G0D5221N,1205322N.

B.V. acknowledges funding from BOF17-GOA-015. J. G. acknowledges funding from DESY P06 and M. M. acknowledges funding from ESRF ID15A.

F.B. acknowledges funding from German Research Foundation DFG grant BR2015/38-1 and the Dr. Rolf M. Schwiete Stiftung.

P.T. acknowledges funding from Ghent University Special Research Fund Grants BOF20/PDO/037 and Research Foundation Flanders grants G0D5221N,1205322N.

M.R. acknowledges the French PICS-CNRS funding program, the French ANR (CLASSY) and the FACCTS program, and funding from the U.S. DOE Office of Science-Basic Energy Sciences, under Contract No. DE-AC02-06CH11357. M.R. and J.C.V. benefited from the Ile de France DIM ACAV+ funding (PARYUGU).

M. Zolotov is supported by NASA grants 80NSSC19K0786 and 80NSSC19K0313.

A. Ts. is supported by Chinese Academy of Sciences President's International Fellowship Initiative, Grant No.2019VCA0004.

D.D. is supported by NASA grants NNX16AL34G and 80ARC017M00005.

E.P. acknowledges funding from Italian Space Agency (ASI) through contract 2018-27-HH-0

F.V., A.H., and C.J. acknowledges funding from NASA's TREX node of the Solar System Exploration Research Virtual Institute 2016 (SSERVI16) Cooperative Agreement (NNH16ZDA001N).

G.D. acknowledges NASA LARS funding of NanoIR technique development (80NSSC19K1051).

M. Zolensky is supported by NASA Hayabusa2 Mission Participating Scientist Program.

M.T. is supported by JSPS KAKENHI Grant Number 21K03654.

C.E., J.D., E.D., and J.M. acknowledge funding from CNES (MIAMI2), DIM-ACAV+ (C3E), LabEx P2IO and ANR (COMETOR ANR-18-CE31-0011)

R.B., A.A., L.R., S.R., and C.P. acknowledge support by the CNES.

K.A. is supported an GP-EES Research Grant.

Author contributions:

Organizing the research, writing the manuscript, main sample analysis: TN

Writing the manuscript, main sample analysis: MM, YE, KA, MZolensky

Electron microscopy: MM, YE, MEZ, TM, DN, MK, AJB, YK, DEB, DJJ, JM, JH, HY, AN, TN, CE, JD, SSR, CM, TT, KT, SY, KY, SA, YA, SDS, TF, TK, FL, TM, HM, AM

Synchrotron experiments: YT, YF, AT, MU, JM, MT, FEB, NJT, LV, MR, JCV, PB, EEA, MT, KF, HS, SY, TK, KI, EB, SE, PT, YT, AT, AT, MY, KU, SO, OS, MS, ED, ED, ZD, ZD, GF, KH, MYH, MK, BL, ML, JZ, BV, DB, BB, FB, KN, JM, IM, RB, AA

Muon analysis: KN, TT, TO, KT, TW, SW, ST, AT, IU, IC, MKK, SN, YM

Physical property measurements: ST, HN, MS, TM, YN, TT, YI, RE, TY, TI, AA, NS, RF, TK

Numerical simulations: HG, MYZ, KK, SW, RH

Reflectance spectra: KA, EK, MM, REM, ET, SS, TH, KK, QHSC, FV, ARH, CJ, DLD, GD, ZG, TK, LR, SR, DT, YY, EP, CP, SMP, CS, CL, RB, AA, KS, GN

TOF SIMS analysis: AD, RJB, IRG

XRD analysis: KS, AJK

Inter-discipline science discussion: HY, RF, HY, HN, KS, ST, HCC, DSL

Hayabusa2 mission sample collection: MY, MY, KY, KY, YY, KY, HY, YY, DY, MY, TY, TY, KW, TU, RT, FT, HT, YT, AI, HS, KS, YS, HS, HS, TS, MO, GO, TO, NO, KO, RN, HN, MN, NN, SN, TM, AAM, AM, YM, KM, KK, TK, SK, KK, SK, TI, YI, MI, HI, SH, RH, CH, YH, NH, NH, TH, MH, KH, SF, RF, AF, YC, MA, MA, SW, YT

All authors discussed the results and commented on the manuscript and meet the journal authorship criteria.

Competing interests: We declare no competing interests.

Data and materials availability:

All images and data used in this study are available at the JAXA Data Archives and Transmission System (DARTS) at https://data.darts.isas.jaxa.jp/pub/hayabusa2/paper/sample/Nakamura_2022/ . Other data on the Ryugu sample and from the Hayabusa2 mission are available at the DARTS archive at https://www.darts.isas.jaxa.jp/curation/hayabusa2 and https://www.darts.isas.jaxa.jp/planet/project/hayabusa2/, respectively. The returned samples are curated and will be distribute by JAXA Astromaterials Science Research Group. Details of sample distribution through Announcement of Opportunity is available at https://jaxa-ryugu-sample-ao.net.

Numerical simulation codes and scripts for the thermal modeling and SPH impact code used in this study are also available at DARTS. The input files used in the iSALE simulations and the output files used to depict figures are also available at DARTS.

Supplementary Materials

Materials and Methods

Supplementary Text

Figs. S1 to S46

Tables S1 to S16

References (*95–194*)

Movies S1 to S2

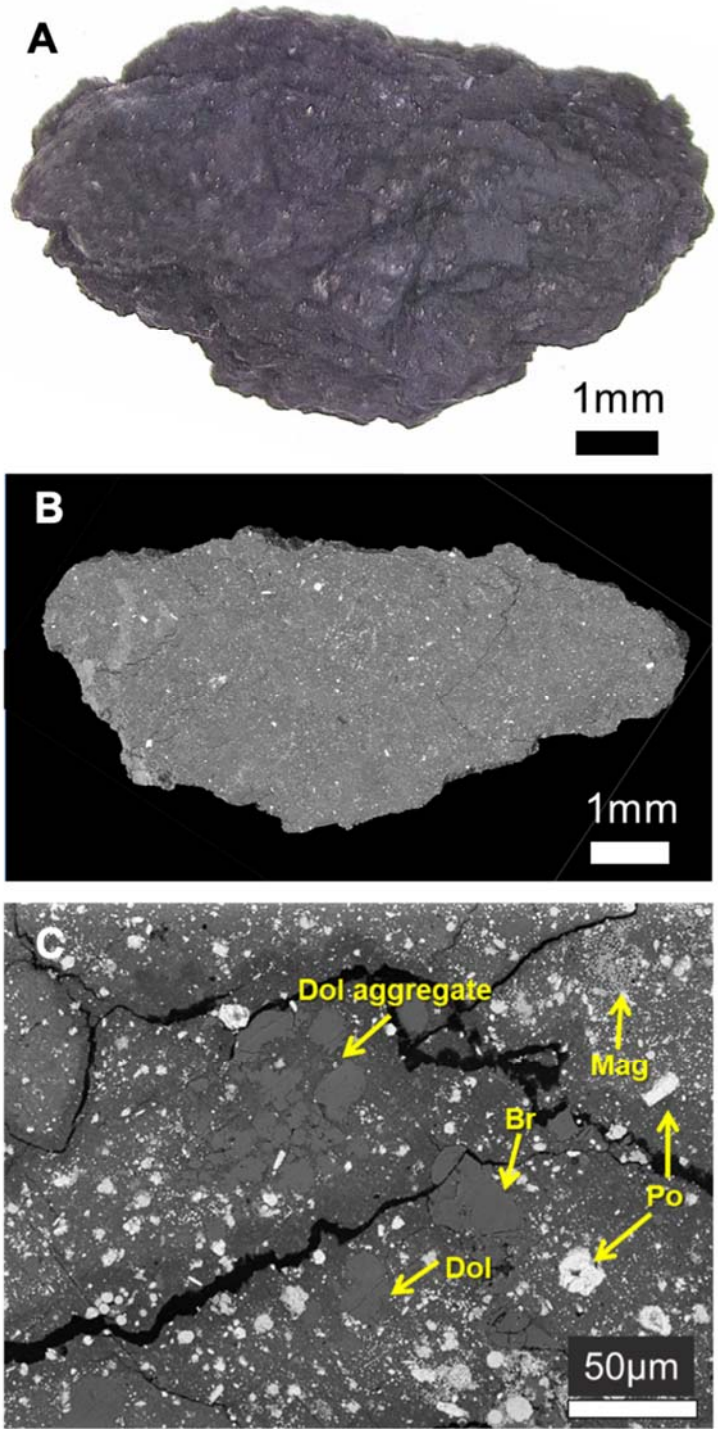

Fig. 1. Morphology and internal texture of C0002. (**A**) Optical micrograph of entire C0002 sample. (**B**) CT image of the largest cross section, showing the absence of chondrules and CAIs. (**C**) Back-scattered electron (BSE) image of typical internal texture**.** Dolomite (Dol), breunnerite (Br), pyrrhotite (Po), and magnetite framboids (Mag) are labelled; these are embedded in a fine-grained phyllosilicate matrix.

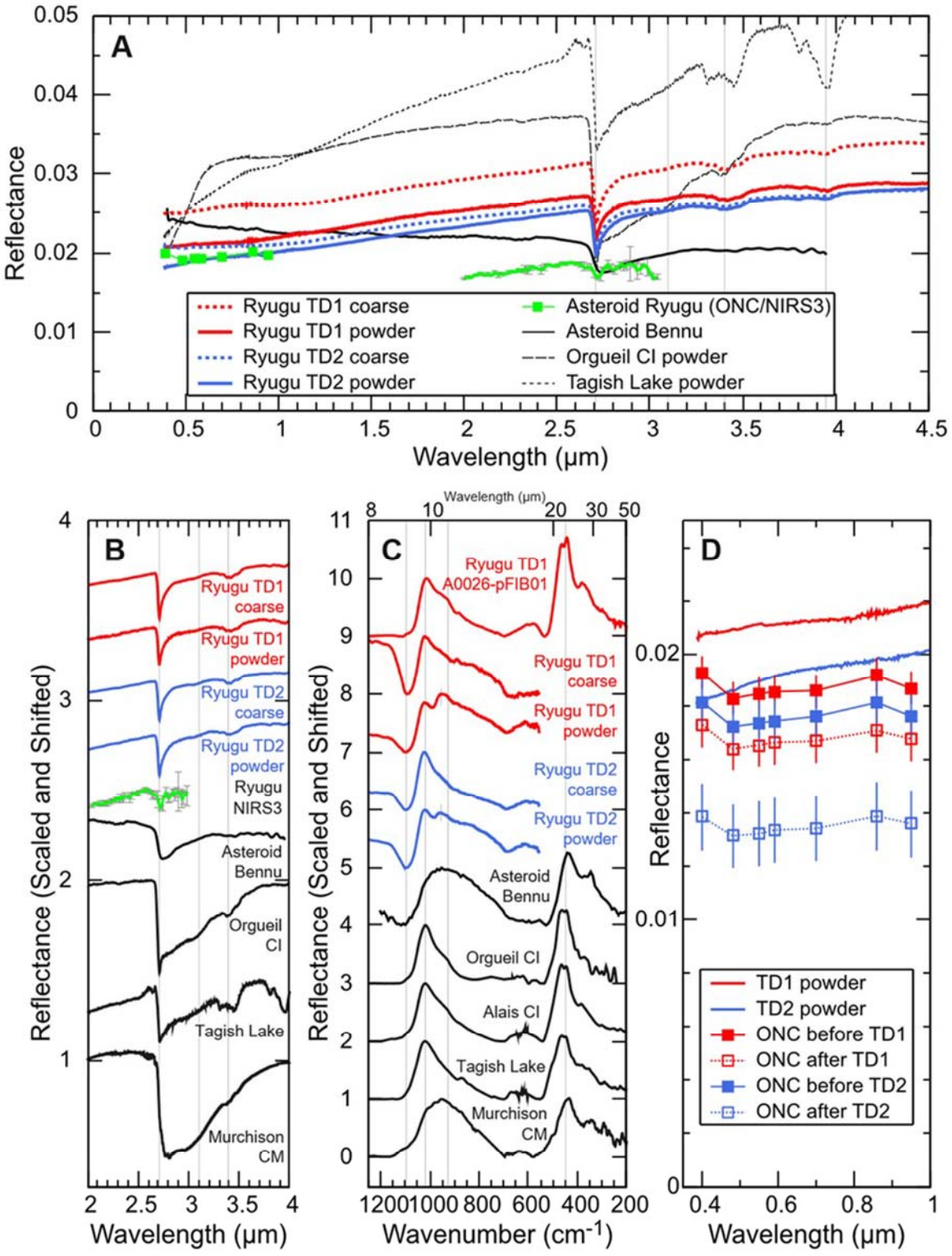

Fig. 2. Reflectance spectra of coarse and powder samples of Ryugu. (**A**) Vis-NIR reflectance spectra of coarse (dotted lines) and powder (solid lines) samples from the TD1 (red) and TD2

(blue) sites on Ryugu, compared to hydrated carbonaceous chondrites (dashed and dotted black lines), Hayabusa2 remote sensing observations of Ryugu (solid green lines) *(2, 3)*, and remote sensing observations of Bennu (solid black line) *(14)*. The vertical gray lines are at 2.71, 3.1, 3.4 and 3.95 µm. (**B**) Same data as panel A, but normalized at 2.595 µm and shifted arbitrary in the NIR wavelength region. (**C**) MIR-FIR spectra of TD1/TD2 coarse and powder samples, the flat surface of sample A0026, remote sensing observations of Bennu (*95*), pressed powders of meteorites (Alais and Tagish Lake), and meteorite coarse samples (Orgueil and Murchison). All spectra are scaled to have the same difference between reflectance minimum and maximum and shifted arbitrary. The vertical gray lines at 9.1, 9.8, 10.75, and 22.3 µm indicate respectively the Christiansen feature, an Si-O stretching peak, an additional shoulder of the main Si-O peak and a peak of the doublet from saponite (*96*). The peaks at 10.5 µm in the powder samples are scattered light from the sapphire dish. (**D**)Visible reflectance spectra of Ryugu TD1/TD2 powder samples measured in the laboratory compared to the TD1/TD2 landing sites before and after the touchdowns *(7)*.

Table 1. Summary of the physical properties measured from the Ryugu samples *(7)*.

Mechanical properties	value	uncertainty	unit	measurement condition	measured sample(s)
compressive hardness	0.18	0.1	GPa	ambient	#C0002 plate 3
Young's modulus	5.3	1.6	GPa	ambient	#C0002 plate 3
bending strength	4.9	1.9	MPa	ambient	C0002 plate 3 and 4
longitudinal velocity	2.08	0.13	km/s	ambient	*avg. of C0002 plate 3 and 4
shear velocity	1.37	0.15	km/s	ambient	*avg. of C0002 plate 3 and 4
thermal expansivity	2.6×10^{-5}	2×10^{-6}	/K	210-400K, nitrogen gas	C0002 plate 3
cohesive force	0.17	0.02	μN	ambient	$C0002 plate 4
Thermal properties					
heat capacity at 298K	865	16	J/kg/K	213-373K, nitrogen gas	avg. of C0002 plate 4 and A0026
thermal diffusivity	3.2×10^{-7}	0.3×10^{-7}	m^2/s	300K, vacuum	avg. of C0002 plate 3 and 4
Electrical properties					
resistivity	2.5×10^{6}	0.3×10^{-6}	ohm・m	300K, vacuum	avg. of C0002 plate 3 and 4
relative permittivity	6.8	0.8	-	300K, vacuum	avg of C0002 plate 3 and 4
Magnetic properties					
magnetic susceptibility	8.39×10^{-5}	4.0×10^{-6}	m^3/kg	300 K, direct current, alternating current (1-1000 Hz)	avg. of C0002 and A0026
saturation magnetization	11.6	5.1×10^{-3}	Am^2/kg	300 K	avg. of C0002 and A0026
saturation remanence	1.05	6.3×10^{-3}	Am^2/kg	300 K	avg. of C0002 and A0026
coercivity	12.2	9.3×10^{-2}	mT	300 K	avg. of C0002 and A0026
coercivity of remanence	61.3	4.1×10^{-1}	mT	300 K	avg. of C0002 and A0026

Average of 26 analysis of fine-grained matrix

* Two fragments from plate 4.

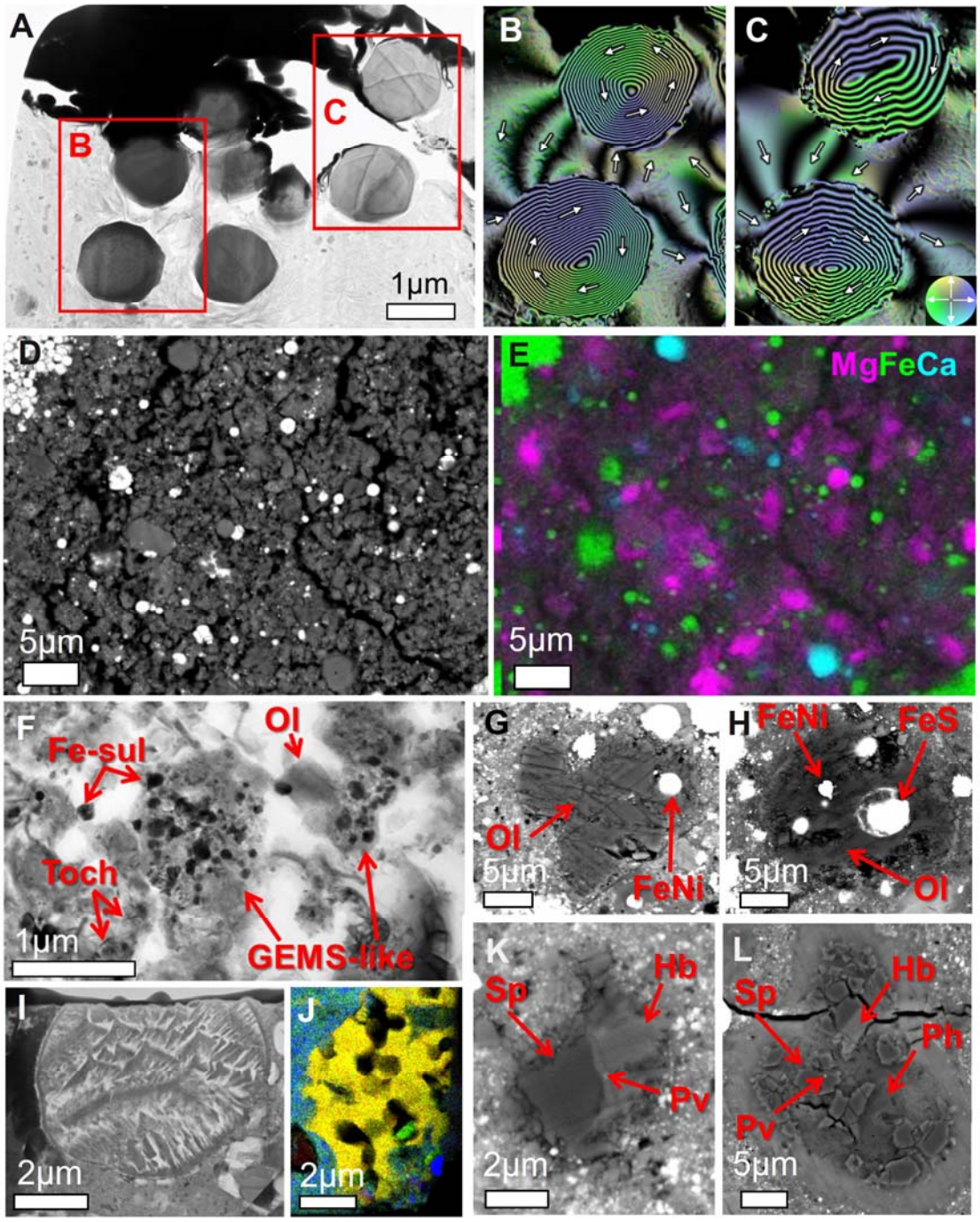

Fig. 3. Characteristic textures, magnetic structures, and embedded objects in the Ryugu samples. (**A)** TEM image of typical magnetite framboids (dark-grey rounded objects) from A0064. The light-grey area is phyllosilicate from the major lithology, and the upper black area tungsten contamination. (**B, C**) Color maps of the magnetic flux direction obtained from the

reconstruction of remanent magnetism, for the magnetite framboids in red boxes in panel A observed using electron holography *(7)*. Each particle has a concentric circular magnetic field (vortex structure) indicated by white arrows, which show the direction of the magnetic flux as shown in the color-wheel in C. Figure S5 shows the composition and electron diffraction data for this region. (**D**) Enlarged view of the least-altered fragment 4 in sample C0002, showing high porosity. (**E**) Compositional map of (C), showing high abundances of Mg-rich olivine and Mg-rich low-Ca pyroxene (magenta), magnetite and pyrrhotite (green), and minor Ca carbonate (light blue). (**F**) TEM image of a part of the least-altered fragment 5 in C0002, showing a very porous aggregate with labelled GEMS-like objects, Fe sulfide (Fe-sul), Mg-rich olivine (Ol), and tochilinite (Toch). (**G, H, I**) Chondrule-like objects. Objects in (G) and (H), both from C0002, show textures similar to type-I chondrules, consisting of Mg-rich olivine (Ol) and an FeNi metal inclusion. An FeS inclusion occurs only in (H). The object in (I) from C0076 shows a barred-olivine texture, consisting of several sets of parallel olivine bars and an olivine rim. (**J**) TEM/EDS color map of a porous olivine (yellow) from C0076, including a small Al, Ti-rich diopside crystal (green). RGB indicates the concentration of Mg, Si, and Fe, respectively. (**K, L**) Small CAIs-like objects. Object in (K) from C0040 consists of Al spinel (Sp), hibonite (Hb), and a small inclusion of perovskite (Pv). Object in (L) from C0002 consists of Al spinel (Sp), hibonite (Hb), a small inclusion of perovskite (Pv) and phyllosilicate (Ph). (A, F, I) are bright-field TEM images and (D, G, H, K, L) are Back-scattered electron (BSE) images.

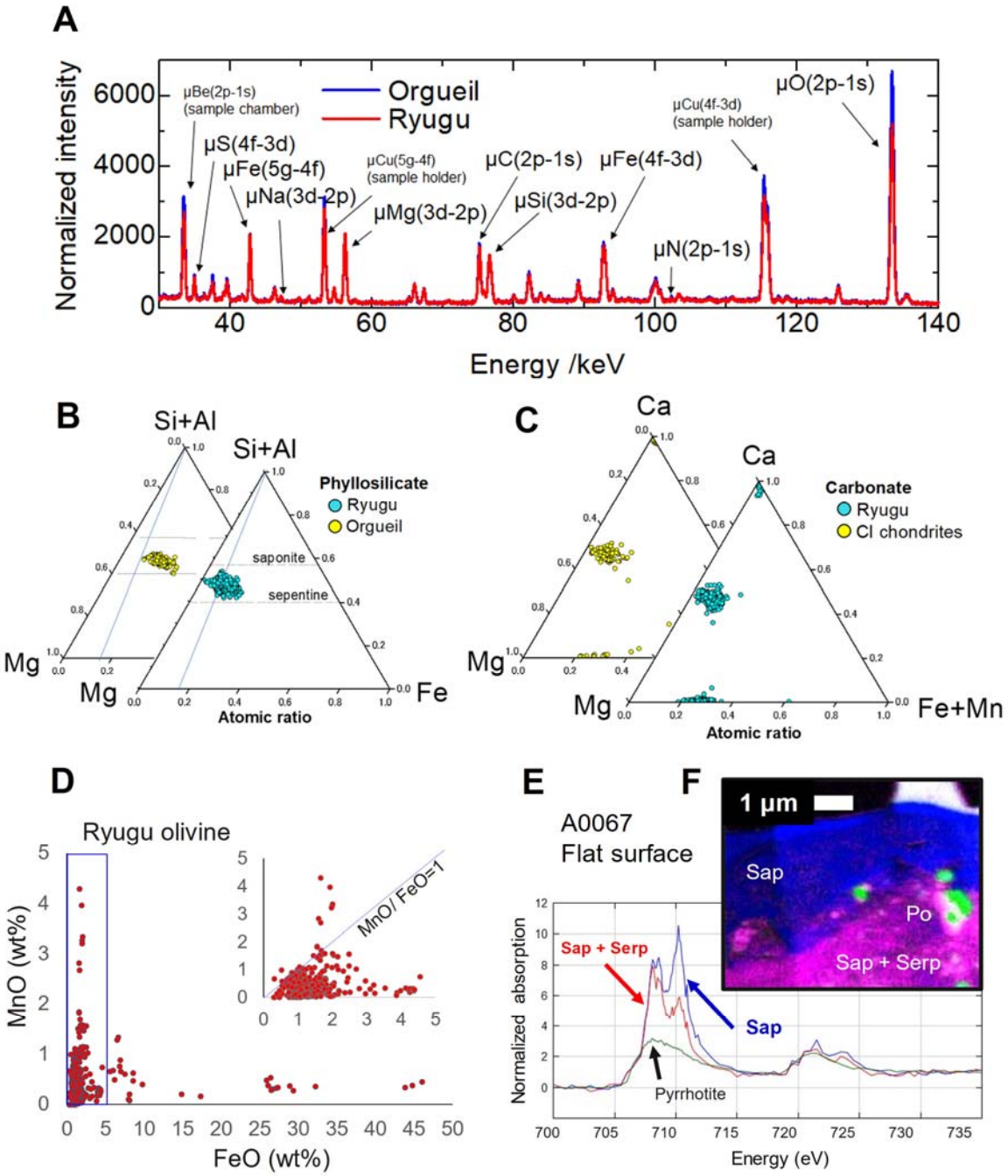

Fig. 4. Results of chemical analyses using muon, electron, and X-ray spectroscopy. (**A**) Normalized muonic X-ray spectra, normalized by μSi 3d-2p X-ray (76 keV) intensities, for Ryugu (red) and Orgueil (blue). μSi 3d-2p X-ray represents the muonic Si X-ray emitted by transition of 3d to 2p muon atomic orbit. (**B**) Ternary diagrams of Mg, Fe and Si+Al, showing the chemical composition of Ryugu phyllosilicates (cyan, 774 analyses), compared with Orgueil (yellow). The blue line corresponds to Mg# = 85. The contribution from FeS was corrected based on S content *(7)*. (**C**) Ternary diagrams of Mg, Ca, and Fe+Mn showing the chemical composition of Ryugu carbonates (653 analyses), compared with CI chondrites (*48*, *52*). (**D**)

MnO and FeO abundances measured from Ryugu olivine (611 analyses). The inset shows an enlargement of the blue box area in the range from 0 to 5 FeO wt%. A blue line indicates MnO/FeO=1 and most olivine data are MnO/FeO<1. (**E**) Fe L2,3-edge XANES (X-ray absorption near-edge structure at Fe L2-edge (706.8 eV) and L3-edge (719.9 eV) regions) spectra of a saponite-rich layer (blue), phyllosilicates of the major lithology (red) and pyrrhotite (green). (**F**) XANES color map of the region shown in Fig. 6B, where three Fe species were found by the singular value decomposition analysis *(97)*, including Fe in saponite (pink), in serpentine-saponite (blue), and in pyrrhotite (green).

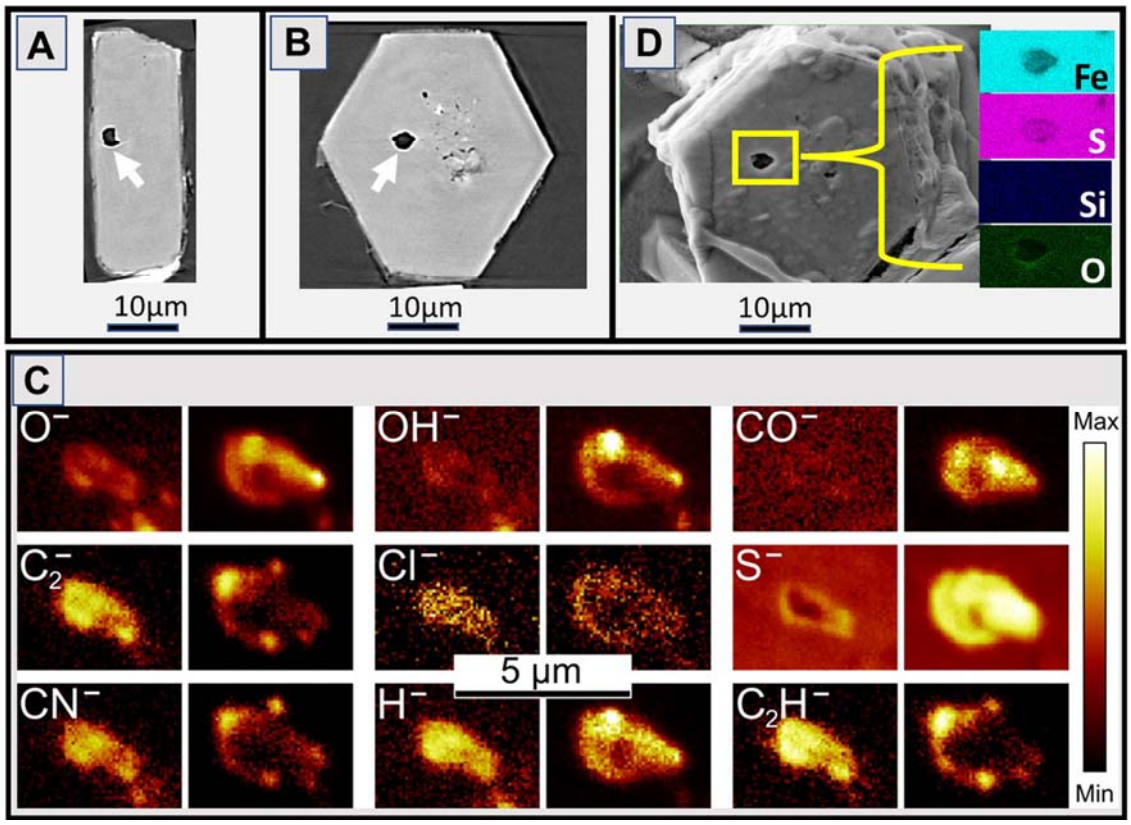

Fig. 5. A fluid inclusion in a Ryugu pyrrhotite crystal. TOF-SIMS and SR-CT measurements were performed on a crystal separated from sample C0002. (**A, B**) Slices through the SR-CT scan, showing the fluid inclusion (arrows) is unconnected to the surface, ~1.5 µm deep in (A). (**C**) TOF-SIMS maps of the fluid inclusion after being frozen (-120 ºC) and opened. Representative secondary ion species are labeled on each image pair, which are measured at the top (left images) and the mid-plane (right images) of the fluid inclusion. OH^- and CO^- are secondary ions of water and CO_2, respectively. S^- is an ion in the aqueous solution. The presence of CN^- indicates N-bearing organic compounds in the fluid, and Cl^- indicates that the trapped fluid was a brine. Differences in the distribution of each species within the inclusion, both within each map and between the top and midplane maps, probably indicate stepwise freezing during sample preparation. (**D**) BSE image of the final surface following the TOF-SIMS measurements, with the opened fluid inclusion in the yellow box. Insets show Fe, S, Si and O element maps of the region within the box, indicating FeS as the host phase.

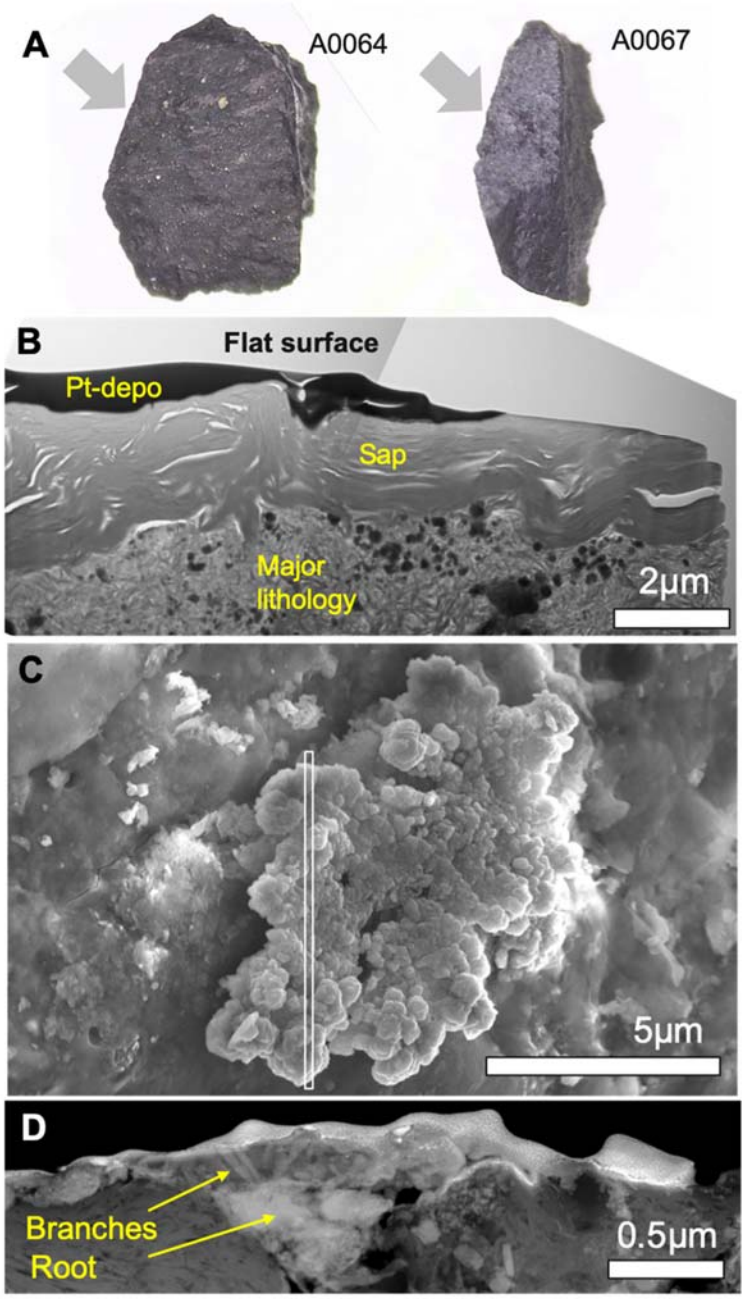

Fig. 6. Flat surface structures and a CuS table coral-shaped object. (**A**) Optical microscope images of flat surfaces (arrows) from two Ryugu samples. (**B**) Depth profile from a TEM image of a slice cut from the flat surface of A0067 to 5 μm depth. The black layer is contamination by Pt coating. A layer of saponite (interlayer spacing d= ~10 Å) makes the surface flat. (**C**) Secondary-electron image of a table coral-shaped CuS object on the flat surface of A0067, formed of a stack of submicron-sized disk-like crystals. (**D**) TEM dark-field image of a slice taken from the white box in (C), perpendicular to the surface to a depth of 10 μm using a focused-ion beam. The object has morphologies similar to a root, several branches, and a stack of disk-like crystals on top. The thin white layer on the top surface of the object is contamination by a Pt coating.

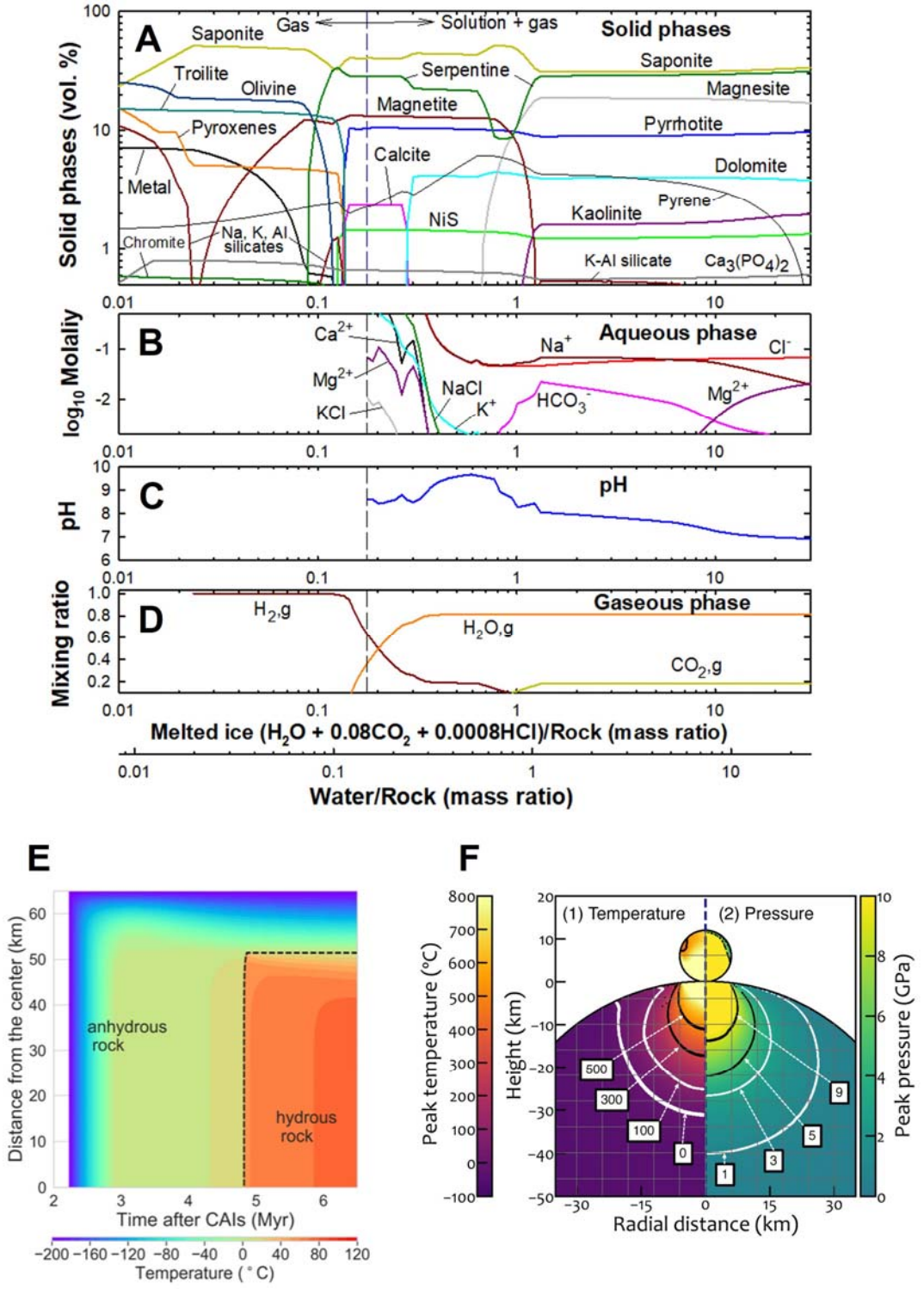

Fig. 7. Calculated models of the aqueous alteration chemical equilibrium, thermal history, and catastrophic impact. (**A**)-(**D**) Model chemical equilibrium of solid, solution, and gas phases during aqueous alteration on the Ryugu parent body at 40 ºC, the pressure of water saturation (7.4×10^{-2} bar), and 10% chemically active organic matter. Each line indicates a

different species or the pH, as labelled. The vertical dashed lines indicate boundaries between aqueous and water-free conditions. Two horizontal scales: melted ice/rock and *W/R*. The ice includes CO_2 and HCl in addition to water and thus the melted ice/rock is larger than the *W/R* (The *W/R* is 0.835 times melted ice/rock). (**E**) Temperature evolution of the Ryugu parent body. The calculation assumes a 65 km radius with *W/R* = 0.6 and formation 2.23 Myr after CAI formation. Color shows the temperature at each location and time. The black dashed line indicates the boundary between the hydrous rock and anhydrous rock, where the highly altered lithology is shifts to the less altered lithology. (**F**) Impact shock model (*7*), with coordinates measured from the center of the parent body. The images show peak temperature (left) and peak pressure (right) at during the impact. The grid of tracer points, placed at multiples of the impactor radius, is shown as grey lines. Isotherms of the peak temperatures are shown as colored curves at 500 ºC, 300 ºC, 100 ºC, and 0 ºC. Isobaric lines of the peak pressures are shown at 9, 5, 3, and 1 GPa. We infer that the material that later accumulated to form Ryugu was further from the impact than the 100 ºC isotherm and the 1 GPa isobar in each panel.